Icarus **141**, 132–155 (1999)
Article ID icar.1999.6154, available online at http://www.idealibrary.com on IDEAL®

Opposition Effect from Clementine Data and Mechanisms of Backscatter

Yu. G. Shkuratov, M. A. Kreslavsky, A. A. Ovcharenko, D. G. Stankevich, and E. S. Zubko

Astronomical Observatory, Kharkov State University, Sumskaya Street, 35, Kharkov 310022, Ukraine
E-mail: shkuratov@ygs.kharkov.ua

C. Pieters

Department of Geological Sciences, Brown University, Providence, Rhode Island 02912

and

G. Arnold

Deutsche Forschungsanstalt für Luft- und Raumfahrt., DLR Institut für Planetenerkundung, Rudower Chaussee 5, D-12484 Berlin, Germany

Received April 9, 1998; revised February 18, 1999

An analysis of Clementine data obtained from a UVVIS camera and simulating laboratory photometric and polarimetric measurements is presented with the use of a new photometric three-parameter function combining the shadow-hiding and coherent backscatter mechanisms. The fit of calculated curves to the average brightness phase function of the Moon derived from Clementine data indicates that the coherent backscatter component is nonzero. The average amplitude of the opposition surge of the Moon in the range of phase angles 0°–1° is approximately 10%. The Clementine data also show a flattening of phase-dependent brightness at angles less than 0.25° that is caused by the angular size of the solar disk. The lunar brightness phase curves at small phase angles are nearly the same in different wavelengths even though at larger phase angles (5°–50°) the lunar surface becomes distinctly redder with increasing phase angle. According to the model, the lack of wavelength-dependent brightness variations at small phase angles can be due to quasifractal properties of the lunar surface. Results of related laboratory measurements suggest that: (1) besides the narrow coherent backscatter opposition spike there is a broad component which can contribute to phase angles up to 10° and (2) a component of coherent backscatter can be important even for low albedo surfaces. The latter testifies the opposition effect of the lunar surface to be substantially formed by the coherent backscatter mechanism.

Key Words: **Moon surface; photometry; regoliths.**

1. INTRODUCTION

Photometry of the lunar surface is a classical branch of planetary physics. Among the problems of lunar photometry, the brightness opposition effect is of special interest. Recent studies of this effect (e.g., Nozette *et al.* 1994, Shkuratov *et al.* 1994a, Buratti *et al.* 1996, Helfenstein *et al.* 1997, Hillier 1997, Hapke *et al.* 1993, 1998) were largely based on (1) obtaining Clementine data and (2) taking new approaches to their interpretation. The latter includes an application of the interference mechanism called often the coherent backscatter enhancement or weak localization of light.

The opposition effect manifests itself as a rapid increase of surface brightness when phase angle α approaches zero. Below about 10° the brightness of the Moon grows more sharply than at large phase angles. The lunar opposition effect is about 1.25 at 1°–10°. Compared to other atmosphereless celestial bodies, the Moon reveals a rather wide opposition surge. Indeed, for asteroids of E-type (Harris *et al.* 1989) and bright satellites of Jupiter (Thompson and Lockwood 1992), the point where the brightness changes from linear growth to a steeply sloped surge is in the range 2°–3°. It is assumed usually that a narrow spike is due to interference enhancement while a wide surge is a result of the shadow-hiding effect (e.g., Mishchenko and Dlugach 1992, 1993, Helfenstein *et al.* 1997). To estimate contributions of both effects at each phase angle α is a difficult problem which is studied recently rather intensively. For instance, Buratti *et al.* (1996) concluded that for the Moon at the phase angles 0°–5°: "... the principal cause of the lunar opposition surge is shadow hiding, while coherent backscatter, if present, makes only a minor contribution." However, Hapke *et al.* (1993, 1998) studying lunar regolith samples have shown the contribution of coherent backscatter to be significant at small phase angles. Helfenstein *et al.* (1997) reached a similar conclusion analyzing telescopic lunar data.

Here we report our findings concerning the lunar opposition effect derived from a detailed analysis of Clementine data. To interpret the results, we use a semiempirical photometric model for regolith-like surfaces (Shkuratov and Ovcharenko 1998) and simulating laboratory measurements in two ranges of phase

0019-1035/99 $30.00

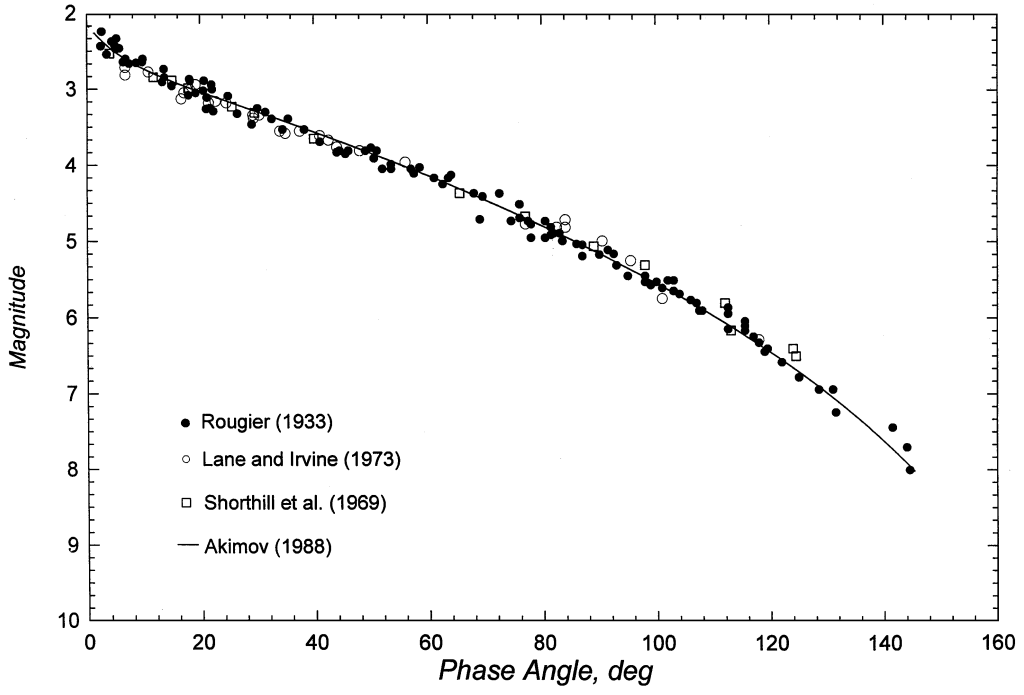

FIG. 1. The integral brightness phase functions of the Moon nearside at 0.45 μm according to Rougier (1933), Shorthill *et al.* (1969), and Lane and Irvine (1973) (symbols) and to the average data by Akimov (1988a) (solid line).

angles, 0.2°–3.5° and 3°–45°. We focus on estimation of contributions of the shadow-hiding and coherent backscatter effects in lunar phase function.

2. SOME REMARKS AND A SHORT REVIEW

Our starting point is a short review of some papers devoted to the opposition effect. This review selects known works as well as rarely-cited ones to correct some stereotyped views on the history of these studies. In addition, we present here a new photometric model used below for processing and interpreting lunar observations.

2.1. Observations

The strong backscatter of light from the Moon at a wide range of phase angles was discovered by Barabashev (1922) by means of the method of photographic photometry. This effect was then studied in detail by his disciple Fedorets (1952). At the time there was the widespread opinion that all surfaces should be approximately described by Lambert's law, which Barabashev and Fedorets showed was clearly incorrect for the Moon. Gehrels *et al.* (1964) were the first to emphasize the opposition effect as a separate phenomenon with possibly a different explanation from the general backscattering property of the lunar surface. Important references up to 1971 can be found in the excellent review by Hapke (1971).

Akimov (1988a), another Barabashev disciple, used his own photoelectric lunar observations carried out during 25 years and the data by Rougier (1933) to propose an integral phase function of the Moon at $\lambda = 0.45\ \mu$m (λ is the wavelength). This function is presented in Fig. 1 together with other data.

Progress in the study of the lunar opposition effect is related to the mapping of its parameters. Wildey (1978) produced an image of the phase ratio $I(2.0^\circ)/I(4.5^\circ)$, where $I(\alpha)$ is lunar surface brightness at a phase angle α. He found interesting features with this image. In particular, the overall mare/highland contrast in this parameter appeared to be very weak. High values of the ratio were observed in regions with moderate albedos. Similar studies of the phase ratio $I(3.2^\circ)/I(14.5^\circ)$ images of the Moon for two spectral ranges ($\lambda = 0.55$ and 0.38 μm) were performed by Akimov and Shkuratov (1981). The ratio $I(3.2^\circ)/I(14.5^\circ)$ at $\lambda = 0.55\ \mu$m is largely higher for regions with intermediate albedo. As to the ultraviolet range, the ratio increases systematically with albedo. Recent studies of lunar phase-ratio images have been carried out by Shkuratov *et al.* (1994a).

The Moon cannot be observed from the Earth at phase angles less than 1° out of eclipse. However, during the Apollo (Pohn *et al.* 1969, 1971, Whitaker 1969, Wildey 1972) and Clementine (Nozette *et al.* 1994, Buratti *et al.* 1996) missions, data on the opposition surge at these small phase angles were obtained. It was found that the brightness ratio $I(0)/I(8^\circ)$ is basically within the limits 1.3–1.4 (Pohn *et al.* 1969, Whitaker 1969). Surface variations of the ratio $I(0)/I(1.5^\circ)$ were also investigated. No correlations with albedo or other surface characteristics were found (Pohn *et al.* 1971, Wildey 1972). Nozette *et al.* (1994) reported that Clementine discovered a narrow lunar opposition spike with amplitude 20% in the last 0.25°. However, as has been shown by Shkuratov and Stankevich (1995) and Shkuratov *et al.* (1997b),

such a spike cannot be observed because the Sun at 1 AU has an angular size of about 0.5°. Each point of the Sun's disk is an independent light source which has its own phase angle. This makes it impossible to observe any details of brightness phase curves the widths of which are less than the angular radius of the Sun. Later Buratti *et al.* (1996) found from Clementine data that: (1) the lunar brightness grows more than 40% between phase angles of 4° and 0; (2) the opposition surge is somewhat larger at 0.41 μm than at 1.00 μm (difference is 3–4%); and (3) the amplitude of the surge depends noticeably on terrain type—it is about 10% greater in the lunar highlands.

2.2. Laboratory Measurements

Laboratory photometric studies of surfaces with complicated structure were started many years ago. In the context of such measurements, the well-known name Ångström (1885) should be recalled. He was a pioneer in laboratory photometry of rough surfaces by visual methods. Barabashov and Chekirda (1945) carried out the first laboratory measurements with a photoelement in a planetology context. From this, precise photometry of simulators of planetary surfaces began.

The first laboratory measurements of the narrow opposition surge were performed by Oetking (1966) who achieved a minimal phase angle about 1°. Oetking measured samples of smoked magnesium oxide (MgO), which possesses a very high albedo. He found that a well-expressed opposition surge with amplitude about 25% started at approximately 10°. It was surprising to find such a surge for a sample with suppressed shadow-hiding effect (Hapke 1966).

The question of how to separate shadowing and the interference effect arose immediately after the first application of this effect in optics of solid planetary surfaces (Shkuratov 1985). Interesting laboratory experiments with lunar samples using linearly and circularly polarized laser light, which were carried out by Hapke *et al.* (1993, 1998), showed that the zero-phase peak of the lunar regolith is caused by both shadow-hiding and coherent backscatter effects in roughly equal amounts. To understand the nature of the narrow and wide opposition surges, laboratory measurements at the phase angles 0.2°–3.5° were performed by Shkuratov *et al.* (1997b). In these measurements, a sample formed by MgO smoked deposits suggested two surperposed opposition surges ($\alpha < 1.5°$ and $\alpha < 10°$), both with amplitudes of about 20%.

2.3. Theoretical Studies

The lunar opposition effect from its discovery almost up to now was explained as being caused by the shadow-hiding mechanism (Hapke 1981, 1984, 1986, Lumme and Bowell 1981a, 1981b, Bowell *et al.* 1989, Hillier 1997). This mechanism is understood rather well, though its rigorous description faces large difficulties, because the theoretical solution of the problem requires estimations of Feynman integrals.

The glory effect (Akimov 1980) and light focusing (O'Keefe 1957, Shkuratov 1983) produced by spherical regolith particles were considered as additional mechanisms of the lunar opposition effect, but at present only interference is recognized as the main rival for the shadow-hiding effect. The history of the mechanism began with the works of Gnedin and Dolginov (1963) and Watson (1969). The first cited paper is devoted to the multiple-scattering problem in quantum physics while the second considers the problem of electromagnetic wave scattering from plasma fluctuations. Since then, this phenomenon has been studied independently by many physicists. There exists a review by Kravtsov and Saichev (1982) on pre-1982 interference enhancement studies. That the interference enhancement can explain the opposition effect of natural surfaces was casually mentioned by Kuga and Ishimaru (1984).

Despite this long and rich history, the interference mechanism was a big surprise for astronomers who studied the opposition effect of celestial bodies. The first "astrophysical" works in this field are Shkuratov (1985, 1988), Muinonen (1989, 1990), and Hapke (1990). Since then, the approach has been intensively developed by Mishchenko (1992) and Mishchenko and Dlugach (1992, 1993). The "interference" explanation for both the opposition effect and the negative polarization was given by Shkuratov (1985, 1988, 1989) and independently by Muinonen (1989). There are reviews on the backscatter phenomena of atmosphereless celestial bodies (Muinonen 1993, Shkuratov *et al.* 1994b).

3. NEW PHOTOMETRIC MODEL

The photometric models by Hapke (1981, 1984, 1986) and Lumme and Bowell (1981a, 1981b) which have been widely used in many works do not take into account coherent backscatter enhancement, although attempts to frame models working with both the shadow-hiding effect and coherent enhancement exist (Shkuratov *et al.* 1991, 1996, 1998, Zhukov *et al.* 1994, Helfenstein *et al.* 1997). These attempts, however, have not yet resulted in a convenient agreed-upon model.

We present here a new heuristic model combining the interference and shadow-hiding effects. This model operates with three parameters. The model is semiempirical because we use approximate simple expressions at the derivation.

3.1. General Description

First, let us describe a model of scattering surface. There are three classes of irregular surface structures. The first can be adequately presented by a random single-connected single-valued function. The second is described by a random single-connected but multiple-valued function. Finally, the third corresponds to disruption of the surface interface. This class is described by random multiple-connected functions. Surfaces of the third class are particulate. They may be considered as media. From the standpoint of the shadow-hiding effect, the second class is close to the third. Actually, in both these cases, surface slopes can

be significant, more than $\pi/2$, and this allows very prominent shadow-hiding phase dependences to be obtained. The proximity of shadow-hiding effects for the last two classes of surfaces is intuitively understandable. Indeed, on section of a random single-connected multiple-valued surface by any plane (e.g., by the scattering plane), a two-dimensional "particulate" medium is formed in this plane. The same will be observed in the case of the third class of surfaces. Thus, in both cases, it is necessary to calculate the shadow-hiding effect in particulate 2D media.

The lunar surface has a complicated structure. The structure is different for different scales. At bases more than 1 cm, the surface can be mainly described by a random single-connected single-valued function. For the scales less than 1 mm, the lunar surface becomes a particulate medium. The lunar regolith surface consists of opaque or semitransparent particles with sizes on the order of $100\,\mu$m; much more than the wavelength of light. In turn, the regolith particles are mainly aggregates of micrometer–submicrometer grains. To describe such a surface, some simplifications are necessary.

Consider a discrete semi-infinite medium consisting of scatterers with sizes of order and less than the wavelength. Suppose that the boundary of the medium has a physical fractal structure created by superposition of many surface undulations at different scales: each large-scale undulation can be considered a reference surface for the next smaller-scale undulation (Shkuratov 1995). Even if each elementary undulation is small, their cumulative effect can be significant, when the number of such undulations is large. This procedure allows obtaining a steep-slope relief. In particular, this relief can be non-single-valued; i.e., it may have slopes steeper than 90°, like in the case of a particulate medium. We suppose that the characteristic scale of the smallest-scale undulation is greater than the size of medium discreteness and the wavelength. This permits using the scattering indicatrix of the semi-infinite medium with the plane boundary to characterize the minimal surface element of the physical fractal structure. For the scale of forming this intrinsic surface indicatrix, we can take into consideration the interference effect. It is necessary to emphasize that discreteness of the acting portion of such a fractal surface can be formed by rather large fragments with intricate structure. It allows modeling of the shadow-hiding effect as if we deal with a particulate medium. This approach makes it possible to avoid traditional problems concerning calculations of the shadow-hiding effect in particulate surfaces (e.g., Hapke 1981, 1986, Hillier 1997). Finally, this permits the simplification of the results. Besides, our model takes into account the actual observed hierarchy inherent in the lunar surface: the smaller the scale of consideration, the larger the average slopes of the surface.

Our model suggests the photometric function in the form $f(\alpha, b, l) = H(\alpha)D(\alpha, b, l)$. The first factor $H(\alpha)$ accounts for strong dependence of the photometric function on α. The second factor $D(\alpha, b, l)$ presents dependences on the photometric latitude b and longitude l. The photometric coordinates (α, l, b) can easily be transformed into traditional coordinates (i, ε, ψ), where i and ε are the angles of incidence and emergence, respectively, and ψ is the azimuth angle—the angle between the plains of incidence and emergence:

$$\begin{aligned} \cos i &= \cos b \cos(l - \alpha) \\ \cos \varepsilon &= \cos b \cos l \\ \cos \alpha &= \cos i \cos \varepsilon + \sin i \sin \varepsilon \cos \psi. \end{aligned} \tag{1}$$

3.2. Coherent Backscatter Enhancement

To estimate the interference effect, we develop an approach suggested by Shkuratov (1988), Shkuratov *et al.* (1991), and Zhukov *et al.* (1994).

Let there be a discrete semi-infinite medium with a flat-on-average boundary. Suppose that the medium consists of rather small scatterers, which have a scattering amplitude a and the isotropic indicatrix. Let a ray from an infinitely remote source cross the boundary at a point 1, the incident angle being i. After multiple scattering in the medium the ray crosses the boundary at a point 2, moving from the medium with the emergent angle ε to an infinitely remote observer. The distance between these points 1 and 2 is s. Let us consider direct and time-reversal light trajectories connected the points 1 and 2 in the medium. The contribution of such trajectories in the scattered electromagnetic field looks like

$$E \sim \zeta_{12} \exp(-i\delta_{12}) + \zeta_{21} \exp(-i\delta_{21}), \tag{2}$$

where ζ_{12} and ζ_{21} are the amplitudes of multiple scattering for the direct and time-reversal trajectories, and δ_{12} and δ_{21} are the corresponding electromagnetic phases. Owing to sphericity of the indicatrix of scatterers, the condition $\zeta_{12} = \zeta_{21} = \zeta$ is valid, $\zeta = a^n$, where n is the multiplicity of scattering ($n \geq 2$). The amplitude ζ does not depend on mutual position of the points 1 and 2. Thus, the intensity of interfering waves which correspond to the direct and time-reversal trajectories is

$$EE^* \sim \zeta\zeta^*(1 + \cos\Delta), \tag{3}$$

where $(^*)$ denotes the complex conjugation and $\Delta = \delta_{12} - \delta_{21}$. The mutual shift of electromagnetic phases Δ for the trajectories depends upon mutual position of the points 1 and 2, which is characterized by vector $\mathbf{S}$ linking the points.

Coherent backscattering enhancement occurs, since near the direction $\alpha = 0$ the trajectories (source) $\rightarrow$ (point 1) $\rightarrow$ (point 2) $\rightarrow$ (observer) and (source) $\rightarrow$ (point 2) $\rightarrow$ (point 1) $\rightarrow$ (observer) are almost equal—photons going along the trajectories interfere constructively. The electromagnetic phase shift described is $\Delta = (\mathbf{k}_i - \mathbf{k}_\varepsilon) \cdot \mathbf{S}$, where $\mathbf{k}_i$ and $\mathbf{k}_\varepsilon$ are the wave vectors of the incident and emergent rays. In a coordinate presentation $\Delta = 2\pi s\lambda/u$, where λ is the wavelength and $u = \sin i \cos\varphi - \sin\varepsilon \cos(\psi - \varphi)$, ψ being the angle between the planes of incidence and emergence and φ being the polar coordinate of $\mathbf{S}$. If $\psi = 0$ and $i = \varepsilon$ (the case when $\alpha = 0$), the value $\Delta = 0$.

One can see that the electromagnetic phase shift Δ does not depend on any properties of the light-scattering medium. Therefore, Eq. (3) holds for all possible trajectories of light crossing the points 1 and 2 and all multiplicities of scattering (of course, excluding the single scattering). Thus,

$$\overline{E}\,\overline{E}^{*} \sim \Theta_{\mathrm{m}}(1+\cos\Delta), \tag{4}$$

where $\bar{E}$ is the sum of fields corresponding to all orders (≥ 2) of scattering and Θ_{m} is the multiple-scattered component of the incoherent ("classical") part of scattered flux. It should be emphasized that this convenient factorized form for the combination of the interference and "classical" effects presented by Eq. (4) is due to sphericity of the scattering indicatrix of medium particles, although at rather small phase angles this is also valid for an arbitrary indicatrix in some approximation.

Equation (4) ignores the vector nature of light. To take into account polarimetric effects, we make use of the vector statement for the reciprocity principle (e.g., Cho 1990). At $\alpha = 0$ we have

$$\left(\mathbf{E}_0 \cdot \mathbf{E}_{12}\right) = \left(\mathbf{E}_0 \cdot \mathbf{E}_{21}\right), \tag{5}$$

where $\mathbf{E}_0$ is the electric vector of incident field, and $\mathbf{E}_{12}$ and $\mathbf{E}_{21}$ are the electric vectors of the scattered field, corresponding to direct and time-reversal trajectories. Equation (5) shows that the copolarized components for these trajectories are the same; i.e., they always interfere constructively. As to the cross-polarized components for the trajectories, they are arbitrary and may interfere both constructively and destructively. This means that in backscattering, the contribution of the cross-polarized components is mainly incoherent. Only for a rather narrow set of "symmetrical" trajectories for which the condition $|\mathbf{E}_{12}| = |\mathbf{E}_{21}|$ is valid as well as Eq. (5) are both co- and cross-polarized components enhanced by interference.

Thus, one may rewrite Eq. (4) as

$$\overline{E}\,\overline{E}^{*} \sim \Theta_{\mathrm{m}}(1+\eta\cos\Delta). \tag{6}$$

The factor $\eta \cong 1/2$ is introduced to account for the interference enhancement only of the copolarized component. For simplicity, we use below the exact equality $\eta = 1/2$.

Let us put the flux photometric function $\chi(\alpha, i, \varepsilon)$ of the medium as

$$\chi(\alpha, i, \varepsilon) = \Theta_1 + \Theta_{\mathrm{m}}\left(1 + \frac{\Omega}{2}\right), \tag{7}$$

where Θ_1 is the single-scattering component and the interference term Ω can be determined as follows:

$$\Omega = \frac{\int_0^{2\pi} d\varphi \int_d^{\infty} \cos\Delta \cdot W(s)\,s\,ds}{2\pi \int_0^{\infty} W(s)\,s\,ds}. \tag{8}$$

A screening factor $W(s)$ characterizes density of the probability that a photon goes from the medium in the point 2, if this photon came to the medium in the point 1. The value d is the size (radius) of the medium volume, in which single scattering is formed. In this volume the coherent backscatter effect cannot occur. In particular, it can be treated as an effective size (radius) of particles, if they are structureless and much larger than λ. If the characteristic size of particles is of the order or less than λ, one can assume that $d \sim \lambda$. The value d is a semiempirical but convenient characteristic.

We describe the dependence of the probability density on s by the function $W(s)$ which presents an energy distribution in scattering spot for an isotropic point source placed in a scattering medium consisting of weakly absorbing particles in the diffusion approximation (Ishimaru 1978),

$$W(s) = \frac{1}{s}\exp\left(-\frac{s}{L}\right), \tag{9}$$

where L is the characteristic scale of light diffusing in the medium. The value L characterizes the attenuation of light from the point source occurred due to absorption and scatter in medium. If a medium consists of slightly absorbing scatterers, L is much longer than the mean free path of light transport in the medium. Integration in Eq. (8) over s gives

$$\Omega = \frac{1}{2\pi}\int_0^{2\pi} d\varphi \frac{\exp\left(-\frac{d}{L}\right)\left[\cos\left(\frac{2\pi d}{\lambda}u\right) - \frac{2\pi L}{\lambda}u \cdot \sin\left(\frac{2\pi d}{\lambda}u\right)\right]}{1 + \left(\frac{2\pi L}{\lambda}u\right)^2}. \tag{10}$$

If phase angles are small enough, the term

$$\cos\left(\frac{2\pi d}{\lambda}u\right) - \frac{2\pi L}{\lambda}u \cdot \sin\left(\frac{2\pi d}{\lambda}u\right) \approx 1. \tag{11}$$

We consider this equality as the exact one to estimate the integral in Eq. (10). In this case, integration over φ yields

$$\Omega = \frac{\exp\left(-\frac{d}{L}\right)}{\sqrt{1 + \left(\frac{2\pi L}{\lambda}\right)^2\left[\sin^2 i + \sin^2\varepsilon + 2(\cos i\cos\varepsilon - \cos\alpha)\right]}}. \tag{12}$$

Calculations show that at small angles i and ε, the value Ω depends on the scattering geometry only slightly; therefore, for approximate estimates we can use any geometry, e.g., the "mirror" one: $i = \varepsilon = \alpha/2$. Then $\sin^2 i + \sin^2\varepsilon + 2(\cos i\cos\varepsilon - \cos\alpha) = 4\sin^2\alpha/2$, and hence

$$\Omega = \frac{\exp\left(-\frac{d}{L}\right)}{\sqrt{1 + \left(\frac{4\pi L}{\lambda}\sin\frac{\alpha}{2}\right)^2}}. \tag{13}$$

We will use this simple approximate expression below in order to describe the component of coherent backscatter enhancement.

The classical solution of the radiative transfer equation for the isotropic indicatrix of elementary scattering volume with single-scattering albedo ω gives the expression for the indicatrix of light flux scattered by the medium (e.g., Ishimaru 1978)

$$\Phi(\alpha, i, \varepsilon) = \frac{\omega}{4} \cdot \frac{\varphi(\omega, i)\varphi(\omega, \varepsilon)}{\cos i + \cos \varepsilon} \cos i \cos \varepsilon, \tag{14}$$

where $\varphi(\omega, \gamma)$ is the Ambartsumian–Chandrasekhar function. Consequently, one can write that

$$\Theta_m(\alpha, i, \varepsilon) \sim \left[\frac{\varphi(\omega, i)\varphi(\omega, \varepsilon) - 1}{\cos i + \cos \varepsilon}\right] \cos i \cos \varepsilon \tag{15}$$

and

$$\Theta_1(\alpha, i, \varepsilon) \sim \frac{\cos i \cos \varepsilon}{\cos i + \cos \varepsilon}. \tag{16}$$

Thus, finally,

$$\chi(\alpha, i, \varepsilon) = \left[1 + [\varphi(\omega, i)\varphi(\omega, \varepsilon) - 1] \times \left(1 + \frac{\exp(-d/L)}{2 \cdot \sqrt{1 + \left(\frac{4\pi L}{\lambda} \sin \frac{\alpha}{2}\right)^2}}\right)\right] \cdot \frac{\cos i \cos \varepsilon}{\cos i + \cos \varepsilon}. \tag{17}$$

If the multiple scattering component dominates total scattered flux (we have suggested this when we considered the coherent backscatter enhancement), then

$$\chi(\alpha, i, \varepsilon) \approx \left(1 + \frac{\exp\left(-\frac{d}{L}\right)}{2 \cdot \sqrt{1 + \left(\frac{4\pi L}{\lambda} \sin \frac{\alpha}{2}\right)^2}}\right) \cdot \frac{[\varphi(\omega, i)\varphi(\omega, \varepsilon) - 1] \cos i \cos \varepsilon}{\cos i + \cos \varepsilon}. \tag{18}$$

We will use this intrinsic indicatrix below.

3.3. *Shadow-Hiding Effect*

Let us consider a random surface arranged as a physical fractal (Feder 1988). This means that the surface is hierarchic and can be expanded on statistically similar structure generations with differing scales. Let the photometric function of such a multi-scale surface be $F(\rho_n, \alpha, b, l)$ where ρ_n is the cumulative slope of the surface, $\rho_n = n\sqrt{\theta^2}$, $\sqrt{\theta^2}$ being the RMS slope for a single structure generation and n being the number of the generations. This function can be represented as

$$F(\rho_n, \alpha, b_0, l_0) = \frac{1}{S_0} \int_{S_n^{(iv)}} \chi[\alpha, b_n(u, v), l_n(u, v)]\, du\, dv, \tag{19}$$

where S_0 is a sufficiently large part of the main reference plane; l_0 and b_0 are the photometric coordinates for the main reference planes; $S_n^{(iv)}$ is the part of the surface both illuminated and visible (iv), simultaneously; u and v are spatial coordinates on this surface; and $\chi[\alpha, b_n(u, v), l_n(u, v)]$ is an elementary flux indicatrix of scattering (the intrinsic photometric function of a particulate surface), l_n and b_n being the local photometric coordinates. The indicatrix can be described, for example, by Eq. (18).

Equation (19) represents an averaging the elementary flux indicatrix $\chi(\alpha, b, l)$ over the part of the surface both illuminated and visible. As a rule, it is very difficult to obtain an explicit expression for the integral (19), and this is the main difficulty of any shadow-hiding theory. However, if one assumes that the surface is formed as the physical fractal, the averaging can be replaced by an equivalent procedure that can be reduced to solving a relatively simple differential equation. Actually, in the case of the physical fractal formed by n generations, one can write that

$$F(\rho_n, \alpha, b_0, l_0) = \frac{1}{S_0} \int_{S_0} F[\rho_{n-1}, \alpha, b(u_0, v_0), l(u_0, v_0)] \frac{du_0\, dv_0}{\cos \theta(u_0, v_0)}, \tag{20}$$

where θ are the local slopes of the structure generation of the largest scale, and u_0 and v_0 are coordinates introduced on the main reference plane.

If n tends to infinity keeping the fractal and topological dimensions equal, we come to mathematical objects named "fractoids" which have been introduced by Shkuratov (1995). The transition from a physical fractal to the corresponding fractoid (Shkuratov 1995) makes it possible to obtain from Eq. (20) the differential equation

$$\frac{\partial F(\rho, \alpha, b, l)}{\partial \rho} = \frac{1}{4}\left(\nabla^2 + 2\right) F(\rho, \alpha, b, l), \tag{21}$$

where ∇^2 is the Laplacian (in the variables b and l) and ρ is the limit of ρ_n when n goes to infinity and θ^2 goes to zero simultaneously (the fractoid definition implies that this limit exists and is not equal to zero). Supplementing this differential equation with proper initial and boundary conditions, one comes to the classical Sturm–Liouville problem on a spherical sector with the following boundaries: $\alpha - \pi/2 \le l \le \pi/2$ and $-\pi/2 \le b \le \pi/2$. Its solution has been presented in detail by Shkuratov (1995) and Shkuratov *et al.* (1994a). The function $F(\rho, \alpha, b, l)$ is expanded in the Laplacian eigenfunctions for the spherical sector,

$$F(\rho, \alpha, b, l) = \sum_{m=0}^{\infty} \sum_{n=0}^{\infty} E_{mn}(\alpha) \cdot \exp\left(-\frac{\rho}{4}(C_{mn}(\alpha) - 2)\right) \cdot \cos\left[k_m\left(l - \frac{\alpha}{2}\right)\right] \cdot (\cos b)^{k_m} \cdot {}_2F_1\left(n + k_m + \frac{1}{2}, -n; \frac{1}{2}; \sin^2 b\right), \tag{22}$$

where $C_{mn}(\alpha) = [k_m(\alpha) + 1/2 + 2n]^2 - 1/4$ and $k_m(\alpha) = \pi(2m+1)/(\pi - \alpha)$, $m = 0, 1, 2, \ldots$. The function ${}_2F_1(a, b; c; x)$ is the hypergeometric polynomials. The coefficients $E_{mm}(\alpha)$ can be found if the initial indicatrix $\chi(\alpha, b, l)$ is known,

$$E_{mn}(\alpha) = \frac{1}{M_{mn}(\alpha)} \int_{\alpha-\pi/2}^{\pi/2} dl \int_0^{\pi/2} db \cdot (\cos b)^{k_m+1} \cdot \cos\left[k_m\left(l - \frac{\alpha}{2}\right)\right] \cdot \chi(\alpha, b, l) \cdot {}_2F_1\left(n + k_m + \frac{1}{2}, -n; \frac{1}{2}; \sin^2 b\right), \quad (23)$$

where

$$M_{mn}(\alpha) = \int_{\alpha-\pi/2}^{\pi/2} dl \int_0^{\pi/2} db \cdot (\cos b)^{2k_m+1} \cdot \cos\left[k_m\left(l - \frac{\alpha}{2}\right)\right] \cdot {}_2F_1\left(n + k_m + \frac{1}{2}, -n; \frac{1}{2}; \sin^2 b\right) = \frac{\pi^2 n!(2m+1) \cdot \Gamma(k_m + n + 1)}{(2k_m + 4\pi + 1) \cdot \Gamma\left(\frac{1}{2} + n\right) \cdot \Gamma\left(k_m + \frac{1}{2} + n\right) \cdot k_m}. \quad (24)$$

For values of ρ greater than 0.3, the series (22) converges very quickly and, therefore, one may save the only term in this expansion. The brightness photometric function, $f(\alpha, b, l) = F(\alpha, b, l)/(\cos l \cdot \cos b)$, looks like

$$f(\alpha, b, l) = H(\alpha) \cos\left[\frac{\pi}{\pi - \alpha}\left(l - \frac{\alpha}{2}\right)\right] \frac{(\cos b)^{\alpha/(\pi-\alpha)}}{\cos l}, \quad (25)$$

where

$$H(\alpha) = \frac{1}{M} \exp\left(-\frac{\rho\alpha(3\pi - 2\alpha)}{(\pi - \alpha)^2}\right) \int_{\alpha-\pi/2}^{\pi/2} dl \int_0^{\pi/2} \chi(\alpha, b, l) \times (\cos b)^{(2\pi-\alpha)/(\pi-\alpha)} \cos\left[\frac{\pi}{\pi - \alpha}\left(l - \frac{\alpha}{2}\right)\right] db, \quad (26)$$

$$M(\alpha) = \pi^{3/2} \left(\frac{\pi - \alpha}{3\pi - \alpha}\right) \frac{\Gamma\left(\frac{\pi}{\pi-\alpha}\right)}{\Gamma\left(\frac{3\pi-\alpha}{2(\pi-\alpha)}\right)}. \quad (27)$$

Note that in the paper by Shkuratov *et al.* (1994a) a misprint was committed. A few formulas describe the latitude dependence as $\cos(\pi b/(\pi - \alpha))$, whereas it should be $(\cos b)^{\pi/(\pi-\alpha)}$.

Equation (26) is rather complicated. Even for simplest initial indicatrices, e.g., for the Lambert scattering law, the final expression is rather cumbersome (Shkuratov 1995, Shkuratov *et al.* 1994a).

3.4. Further Simplification of the Model and Illustrations

A comparison of the function $H(\alpha)$ calculated for a few types of intrinsic indicatrix given by Eq. (18) with experimental phase functions shows that the calculated $H(\alpha)$ falls too sharply at $\alpha > 40^\circ$ for any ρ. This occurs for two reasons. The first is that the phase functions of the hierarchy-arranged multivalued fractal-like surfaces are actually somewhat steeper than in the case of typical particulate media. The second reason is that we do not incorporate multiple scattering between elements of the fractal-like surface in the model. This scattering should diminish the shadow-hiding effect essentially at large phase angles. The simplest way to avoid these shortcomings is to exploit a semiempirical expression for $H(\alpha)$. We suggest the use of

$$H(\alpha) = \frac{\exp(-k\alpha)}{2 + \exp\left(-\frac{d}{L}\right)} \left(2 + \frac{\exp\left(-\frac{d}{L}\right)}{\sqrt{1 + \left(\frac{4\pi L}{\lambda} \sin\frac{\alpha}{2}\right)^2}}\right), \quad (28)$$

where k is a formal parameter close in some sense to ρ.

The idea of using $\exp(-k\alpha)$ to describe the shadow-hiding effect was suggested by Akimov (1980). The coefficient k takes into account diminution of the shadow-hiding effect due to multiple scattering. We assume that the coefficient k depends on albedo A as $k = k_0(1 - A)$, where k_0 is a function of surface geometry characteristics and does not depended on albedo (Akimov 1980). Other simple empirical expressions can also be used to approximate the function $H(\alpha)$. For example, if we deal with particulate media covered by a semitransparent slab of small particles, the function $\exp(-k\alpha)$ is not optimal to describe the shadow-hiding effect (Hillier 1997, Stankevich *et al.* 1999). In this case it is necessary to use a function which is nonlinear on a logarithmic scale.

The part describing brightness distribution over the lunar disk (see Eq. (25)),

$$D(\alpha, b, l) = \frac{\cos\left[\frac{\pi}{\pi-\alpha}\left(l - \frac{\alpha}{2}\right)\right]}{\cos l} \cdot (\cos b)^{\alpha/(\pi-\alpha)}, \quad (29)$$

has no parameters (like the Lambert or Lommel–Zeeliger laws). It presents dependences on the photometric latitude b and longitude l for fractal-like surfaces (Shkuratov 1995). Note that the expression (29) was suggested earlier by Akimov (1975, 1988a, 1988b) and we often name it Akimov's formula.

Thus, finally, we use the semiempirical photometric function

$$f(\alpha, b, l) = \frac{\exp(-k\alpha)}{2 + \exp\left(-\frac{d}{L}\right)} \left\{2 + \frac{\exp\left(-\frac{d}{L}\right)}{\sqrt{1 + \left[\frac{4\pi L}{\lambda} \sin\left(\frac{\alpha}{2}\right)\right]^2}}\right\} \times \frac{\cos\left[\frac{\pi}{\pi-\alpha}\left(l - \frac{\alpha}{2}\right)\right]}{\cos l} \cdot (\cos b)^{\alpha/(\pi-\alpha)}. \quad (30)$$

It has been published without derivation by Shkuratov and Kreslavsky (1998) and Shkuratov and Ovcharenko (1998). Remember that the angles α, b, and l are in radians.

From Eq. (30) the integral phase function can be derived:

$$F(\alpha) = \frac{2}{\sqrt{\pi}} \cdot \frac{\exp(-k\alpha)}{2+\exp\left(-\frac{d}{L}\right)} \left(2 + \frac{\exp\left(-\frac{d}{L}\right)}{\sqrt{1+\left(\frac{4\pi L}{\lambda}\sin\frac{\alpha}{2}\right)^2}}\right) \times \left(1-\frac{\alpha}{\pi}\right)\frac{\Gamma\left(\frac{3\pi-\alpha}{2(\pi-\alpha)}\right)}{\Gamma\left(\frac{4\pi-3\alpha}{2(\pi-\alpha)}\right)}. \quad (31)$$

Equation (31) can in particular be used to interpret asteroid observations. To illustrate this, we present results of fitting model curves to observations of the E-type asteroid 64 Angelina (Harris *et al.* 1989) in Fig. 2 and Phobos (Avanesov *et al.* 1991) in Fig. 3. Brighter 64 Angelina is characterized by suppressed shadow-hiding ($k = 0.62$) and larger light-diffusion volume ($L = 9.06\,\mu$m) than darker Phobos ($k = 1.36$, $L = 3.97\,\mu$m). The different values of d for Phobos ($d = 0.5\,\mu$m) and 64 Angelina ($d = 4.14\,\mu$m) can be treated as a difference between the average size and albedo of regolith particles of these bodies.

We also use Eq. (31) to understand the influence of the model parameters on phase dependences (Fig. 4). As one can see, growth of the parameter L leads to increasing the opposition effect amplitude and its narrowing. When d increases, the amplitude decreases. Variations of k result in total steepness of phase function: the larger the k, the steeper the curves. Note that Eq. (30) predicts a decrease of the phase function slope at very small phase angles. This decrease is absolutely natural for any diffraction phenomena. However, the factor $\exp(-k\alpha)$ can partially compensate this effect.

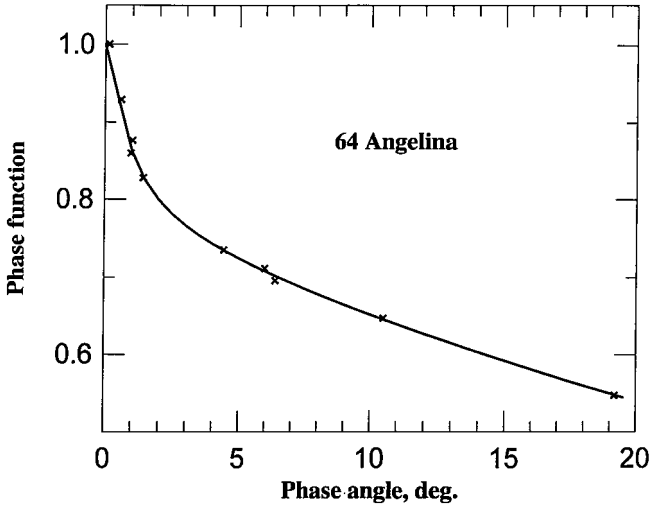

FIG. 2. An illustration of fitting by Eq. (31). Observational data for asteroids 64 Angelina (Harris *et al.* 1989) and the best fit with Eq. (31): $L = 9.06\,\mu$m, $d = 4.14\,\mu$m, and $k = 0.62$.

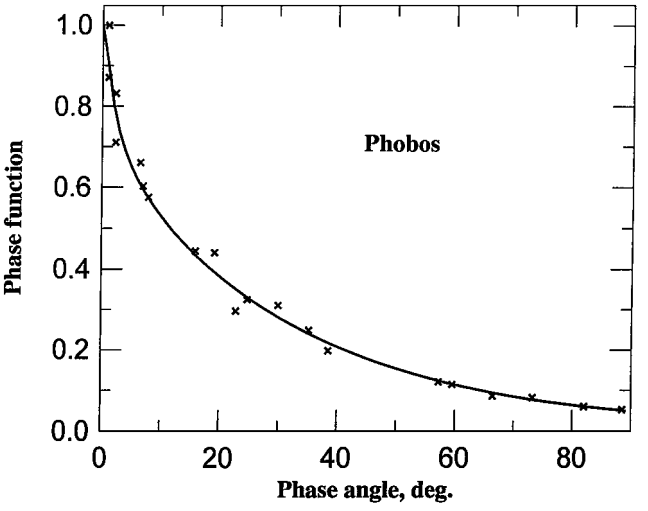

FIG. 3. An illustration of fitting by Eq. (31). Observational data for Phobos (Avanesov *et al.* 1991) and the best fit with Eq. (31): $L = 3.97\,\mu$m, $d = 0.5\,\mu$m, and $k = 1.36$.

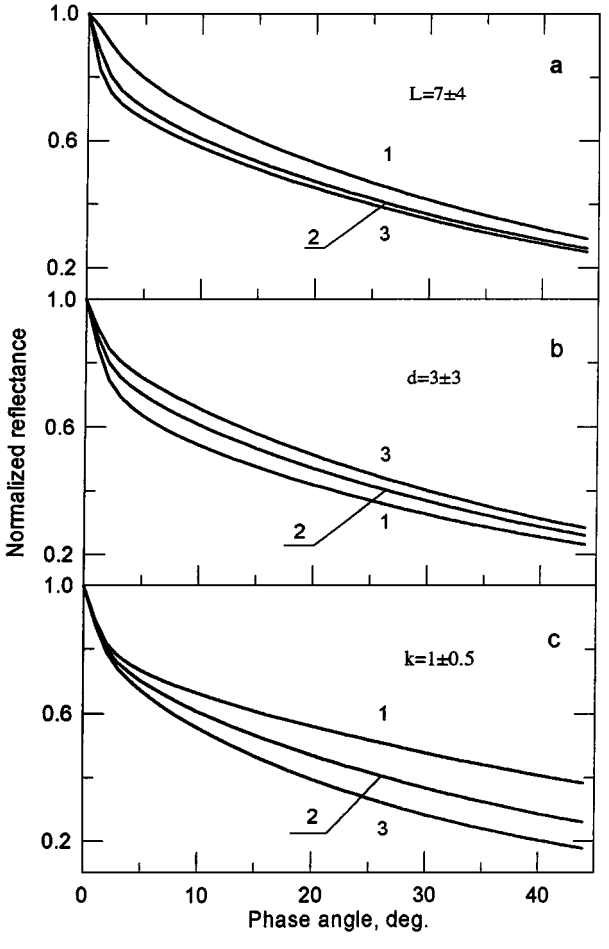

FIG. 4. Results of calculations by Eq. (31) for different values of the model parameters. As a basis set the following values of the parameters are used: $L = 7\,\mu$m, $d = 3\,\mu$m, and $k = 1$ (curve 2 in all plots). The curves 1 and 3 correspond to the cases $L = 3$ and 11 μm (plot a), $d = 0$ and 6 μm (plot b), and $k = 0.5$ and 1.5 (plot c).

One must pay attention to an important case. If the conditions $L \propto \lambda$ and $d \propto \lambda$ are met, the opposition spike has no spectral dependence. The conditions are satisfied, if the medium possesses quasifractal properties, when the surface structure remains the same in some sense independently on variations of λ (i.e., on variations of the "consideration" scale).

The function (30) is used below for processing and interpretation of Clementine data and to analyze results of our laboratory measurements.

4. LUNAR PHOTOMETRY FROM CLEMENTINE IMAGES

In this section we present some results of our study of photometric properties of the lunar surface with images acquired by Clementine spacecraft with the UVVIS camera. We focus here on conclusions about nature of the opposition effect of the lunar regolith. Details of the data processing and extended review of the results will be published elsewhere (M. A. Kreslavsky *et al.*, manuscript in preparation).

As has been noted above, the illumination/observation geometry is described by three angular parameters: α, l, and b. For observations from the Earth, for each point of the lunar nearside, parameters l and b are close to selenographic longitude and latitude. For the regular Clementine mapping, the surface was observed approximately from the local zenith, that is, under $b \approx l \approx 0$. However, a few sites were imaged under other illumination/observation geometries.

UVVIS camera images were taken in the visible and near infrared range. In this work we analyze images taken with the filters A (0.41 μm), B (0.75 μm), and D (0.95 μm). We expect the photometric characteristics of the lunar surface in the filters C (0.90 μm) and E (1.00 μm) to be very close to those in the filter D (0.95 μm) (Nozette *et al.* 1994).

In the following subsections we present average phase functions for the Moon at the phase angles 3°–50° in the three spectral bands 0.41, 0.75, and 0.95 μm; an example of surface brightness dependence on all three geometrical parameters for one site; and examples of phase functions at the phase angles 0°–2°.

4.1. Average Phase Function at 3°–50°

The regular lunar mapping lasted about 2 months. Pairs of orbits separated by approximately 1 month followed close traces on the surface. As a result, a set of stripes on the lunar surface was observed twice under different phase angles. This makes it possible to derive the phase function of the lunar surface from a large set of image pairs at different phase angles (Kreslavsky *et al.* 1997). This approach presented below could be named the method of linked phase slopes.

We restricted the analysis to the latitude zone of the Moon between ±50° and to the phase angle range of 3°–50°. At higher latitudes and large phase angles the Sun is always low and local topography influences the apparent brightness too much. For smaller phase angles a special processing is necessary (see below).

We listed all pairs of overlapping images obtained during the regular mapping under standard viewing geometry, when the camera was directed downward. Then, coordinates of rectangular areas, where images from each pair overlap, were calculated. We found that accuracy of known coordinates of image corners is not enough to match the images. For several randomly selected pairs, error in matching by ballistic data is of order 15–20 image elements. Automated computer procedures for matching gave bad results, because at different phase angles the most contrasted features on the images (e.g., craters) have a different look. On the other hand, the number of pairs is huge and it is absolutely impossible to match images just on a computer screen. Thus we did not compensate errors resulting from inaccuracy of camera pointing data. Pairs for which overlap area was less than 10% of image (that is, the pairs most sensitive to errors in superposition) were excluded. We believe that the errors vanish when data are averaged over a huge number of frame pairs. Thus, for each filter we listed about 10,000 pairs of overlapping frames, where phase angle difference was greater than 3°.

All images from the pairs were decompressed and then calibrated. The calibration developed by the Brown University team was used. We applied all three additive corrections, dividing by the exposure duration and the flat field correction. In the result, images calibrated in counts per millisecond were obtained. We did not perform the absolute calibration, because it was not necessary for derivation of the phase function. For the overlapping rectangle of the calibrated images we calculated the mean brightness and its standard deviation. The mean brightness was corrected for deviation of the photometric longitude l from zero using the longitudinal multiplier from Eq. (30). We excluded those pairs where the difference between the variances (the standard deviation divided by the mean) was abnormally high. The ratio of the mean brightness for two images in each pair gave us the phase ratio for the corresponding phase angles. From this huge set of the phase ratios we reconstructed average phase curves for each spectral band. Our reconstruction procedure minimized a sum of squares of deviations of approximated phase ratios from measured ones. Each phase ratio was weighted with the area of the corresponding overlapping rectangle.

The average lunar phase function for the B filter is presented in Fig. 5 (symbols). It can be approximated with great accuracy by Eq. (30) (solid line in Fig. 5). Unfortunately, a large volume in the space of parameters k, d, and L provides a good fit. Behavior of the phase function at the smallest phase angles can give additional constraints on the parameters. Good agreement with small-phase-angle data, which we obtained for a few sites (see below), can be achieved when $d/\lambda = 1.5$. Values of the parameters k and L providing the best fit under this constraint in the three spectral bands are listed in Table I. One can see that k increases and L decreases with decreasing λ. This result is physically obvious: with decreasing wavelength the albedo decreases; this leads to growth of k (due to diminishing the multiple scattering)

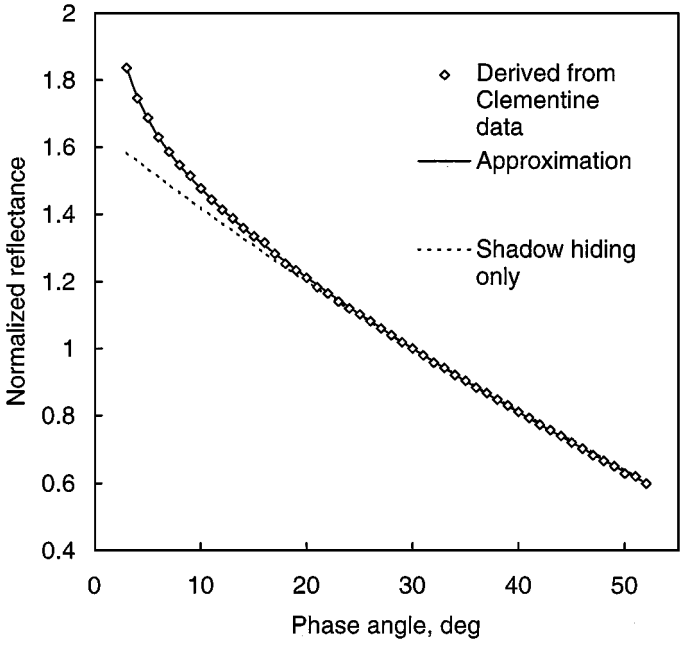

FIG. 5. The average brightness phase function of the Moon derived from Clementine data at 0.75 μm by the method of linked phase slopes (symbols). The line is the best fit by Eq. (30). The parameters values are $L = 4.51$ μm, $k = 0.871$, and $d = 1.12$ μm. The dashed line corresponds the pure shadow-hiding component.

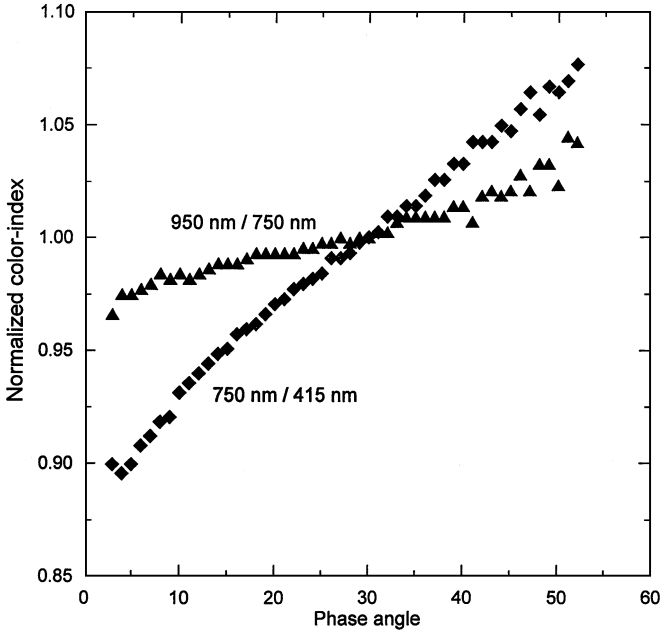

FIG. 6. The average normalized phase dependences of color index C(0.750/0.415 μm) and C(0.95/0.75 μm) of the Moon derived from Clementine data.

and to shortening of the light diffusion length L. Our estimation shows that the variations of k (remember that $k = k_0(1 - A)$) are in quantitative accordance with spectral variations of albedo A. To estimate relative contributions of the shadow-hiding and coherent backscatter enhancement effects, we omitted the interference multiplier in Eq. (30) and then calculated the pure shadowing dependence. The result is presented in Fig. 5 by the dashed line. As one can see, for the wavelength 0.75 μm the relative contribution of the coherent backscatter enhancement is about 15% at the phase angle 3°. Moreover, it is clearly seen that the interference component of the lunar phase dependence occupies a rather wide range of phase angles. Existence of broad coherent backscatter surges is confirmed also by our laboratory measurements (see below).

The average Clementine phase dependences of spectral ratios, or the normalized color indices C(0.75/0.42 μm) and C(0.95/0.75 μm), are given in Fig. 6. A monotonic rise of the color indices is observed: the lunar surface becomes redder with increasing phase angle. This is in agreement with the Earth-based observations of the Moon by Mikhail (1970) and Lane and Irvine (1973), but was not reproduced in some laboratory measurements of lunar samples at phase angles less than 10° (Akimov *et al.* 1979, Shkuratov *et al.* 1996; Hapke *et al.* 1998; see below).

TABLE I
Spectral Dependence of the Model Parameters k and L at $d/\lambda = 1.5$

λ, μm	K	L, μm
0.415	1.042	1.38
0.750	0.871	4.51
0.950	0.813	5.79

The monotonic behavior of the average lunar color indices C(0.75/0.42 μm) and C(0.95/0.75 μm) at phase angles less than 10° can be interpreted in terms of Eq. (30). Actually, if one suggests that the ratio $L(\lambda)/\lambda$ and $d(\lambda)/\lambda$, which are the main parameters of the coherent backscatter mechanism, are nearly constant, the behavior is a function of k, which is a monotonic function of albedo and, consequently, of wavelength. In other words, for the Moon the coherent backscatter enhancement is not vanishingly small; however, in this case the growth of the characteristic interference base is almost compensated for by increasing the wavelength.

4.2. Dependence of Brightness on Photometric Latitude and Longitude

In addition to the regular mapping of the lunar surface with the observation geometry corresponding to $b = l = 0$, Clementine studied a few regions with different viewing angles. This gives a good opportunity to check the dependence on l and b predicted by Eq. (30). Also, it allows us to find the phase dependences for particular regions and to compare them with the average lunar phase function.

As an example, we present here the results for a region close to the Apollo 15 landing site. A small topographically even area shown in Fig. 7 was selected for the analysis. Clementine took

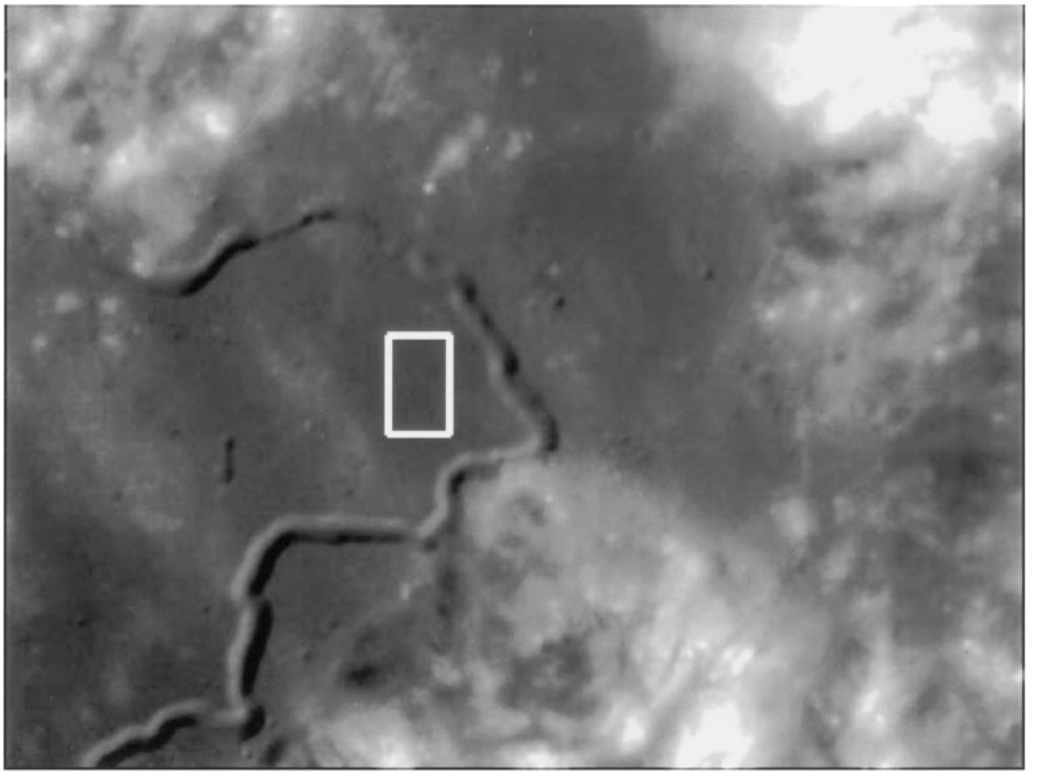

FIG. 7. The Clementine image LUE3909L.299 (filter E, $\lambda = 1.00$ μm) of the vicinity of Apollo 15 landing site. The scene is centered at 26.2°N, 3.4°E. Marked is the area for which the photometric measurements are presented in Fig. 8.

a large series of images of this region at different angles α, b, and l. Brightness of the area in this series of images is plotted in Fig. 8 as a function of α. In the series the phase angle initially decreases and then increases, producing two branches on the brightness dependence. Brightness of the two branches is different for the same phase angles because the other two angles b and l are different. In order to correct for the dependence on photometric latitude and longitude, we divided the measured brightness by Akimov's function $D(\alpha, b, l)$ (see Eq. (29)). This brings the data to the uniform observation geometry ($\alpha, b = 0, l = 0$). The result is presented in Fig. 8. One can see the two branches now coincide. This demonstrates, on the one hand, that Eq. (29) provides a good description of the surface reflectance and, on the other hand, the good photometric quality of the Clementine data. The resulting phase dependence is almost linear and is in agreement with the average lunar data. The data presented in Fig. 8 correspond to the filter E (1 μm). For the shorter wavelengths, the branches after the correction do not coincide so well, but the difference never exceeds 3%.

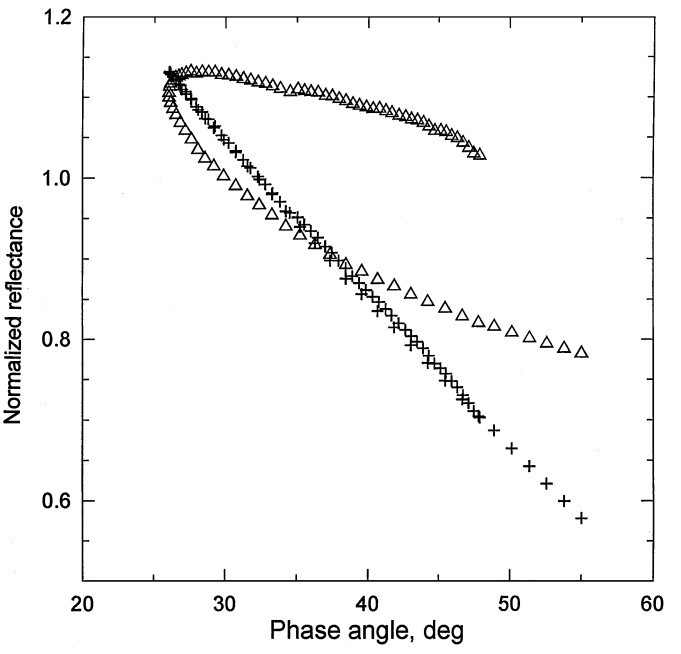

FIG. 8. Normalized reflectance of the area marked in Fig. 7 at different observation geometry plotted against the phase angle (triangles). These data are extracted from 88 frames obtained by Clementine UVVIS camera in filter E ($\lambda = 1.00$ μm). The same data corrected for observation geometry using Eq. (29) are presented by pluses—these present the phase function of the site shown in Fig. 7.

4.3. Opposition Spike

Among images of the lunar surface taken by the UVVIS camera during the Clementine mission there are images including the zero phase angle point or, in other words, the spacecraft shadow point. It gives a unique opportunity to study the lunar opposition spike. This spike is clearly seen in the images as a diffuse bright

spot around the zero phase angle point (Nozette *et al.* 1994). Images of such a kind were also taken during the Apollo 8 (Pohn *et al.* 1969) and other Apollo missions. As an example, Fig. 9a shows the frame LUC2275J.167 (0.90 μm filter). The image is centered at 1.3°N, 3.9°E, and includes the northeast part of Sinus Medii. This region is brightened by the ray system of Crater Triesnecker.

To extract the phase function using images with the spacecraft shadow point, different methods have been used. For instance, Nozette *et al.* (1994) and Buratti *et al.* (1996) suggested using a simple averaging over a number of different images to diminish regional albedo variations. We use other approaches to extract the phase function from Clementine data (Shkuratov *et al.* 1997a, Kreslavsky *et al.* 1998).

Due to spacecraft motion the zero-phase-angle point moved on the surface between consecutive images. Thus, after mutual subtraction (or division) of registered images taken in filters close to each other, the albedo pattern of features is practically eliminated, but the opposition spot is not quenched completely due to the shift of the spacecraft shadow point. Figure 9b shows a contrasted composite image—the result of dividing of the frame LUD2271J.167 (0.95 μm) by the frame presented in Fig. 9a (0.90 μm). One can clearly see in Fig. 9b a specific pattern related to the opposition spot, though the difference in the local phase angle for any point in this composite image does not exceed 0.2°. Knowing the phase angle in each point of both images we calculated the logarithmic derivative of the phase function in each point of the frame. Then we averaged the derivative over all points with the same phase angle. Integration of the derivative provides a phase curve. As a rule, integrating procedures suppress experimental noise and, therefore, our resulted dependences (see Fig. 10) are smooth enough. The curves 1 and 2 correspond, respectively, to the mentioned pair of images and the pair of frames LUD3742J.150 and LUC3746J.150. The latter pair is centered at 1.4°N, 48.7°E, in Mare Fecunditatis.

As one can see, the opposition effect of the Moon at the phase angle 0.2°–1.6° is rather inert with flattening at very small phase angles $<0.25°$. This flattening is due to the angular dimension of the Sun's disk (Shkuratov 1991, Shkuratov and Stankevich 1995). For comparison we also present in Fig. 10 the phase dependences adopted from Buratti *et al.* (1996). These dependences present the mare (curve 3) and highland (curve 4) regions in average. The pronounced surges at phase angles $<0.5°$ observed in the Buratti *et al.* (1996) data may be due to their different approach to analysis.

4.4. Spectral Dependence of Opposition Spike

The approach to study the opposition effect presented in the preceding section is rather accurate, but it does not allow derivation of information about the spectral dependence of the phase function from the Clementine data set. In this section we consider another method for studying the opposition spots, the method of phase-ratio image. It enables the determination of the spectral behavior of the lunar phase function near opposition from the Clementine data (Kreslavsky *et al.* 1998). The method is like that applied to Earth-based telescope images of the Moon (Wildey 1978, Akimov and Shkuratov 1981, Shkuratov *et al.* 1994a). A phase-ratio image is prepared by dividing small- and large-phase-angle images of the same region of the lunar surface. This allows compensation of major albedo variations, although some artifacts originating from surface relief are introduced.

There are a few UVVIS images where this direct comparison is possible. The image shown in Fig. 11a (frame LUA1983J.168 (0.415 μm)) is one of them. Coordinates of its center are 1.4°N and 1.3°E. One can see the crater Blagg at the lower left of the scene. We used the complementary image LUA0598J.300 (0.415 μm) taken at a phase angle of about 26° to calculate the phase-ratio image. The results are presented in Fig. 11b (dark shades correspond to low values of the ratio). Then, we average the phase ratios over all points which have the same phase angles at the small-phase-angle image excluding crater walls and other tilted areas. In this way we obtained average phase curves in blue, red, and IR filters (see Fig. 12). In this case, the brightness is referred to a phase angle of about 26°. At the smallest phase angles the averaged area is small, statistics are poor, and the results are not reliable.

In Fig. 11b some weak variations of the phase ratio, which are not related to changes of phase angle and relief slopes, are seen. These are actual variations of the opposition spike characteristics. They depend on albedo and structure of the regolith. In particular, small bright craters have comparatively low values of the ratio. In terms of Eq. (30), this implies rather high values of L and/or d. In turn, these can result from large average size of regolith particles in the craters.

As one can see (Fig. 12), there is no wavelength dependence of the opposition spike for the phase angle range 0°–1.4°: all these curves are almost parallel. However, at larger phase angles there is a distinct wavelength dependence which affects the magnitude of these normalized reflectances: the phase ratio $I(1°)/I(26°)$ is greater at shorter wavelengths. The average phase dependences derived from Clementine data for the phase angle range 3°–50° also show this behavior (see Fig. 6). This independent approach confirms similar results of Burrati *et al.* (1996). The fact that no conspicuous wavelength dependence of the phase curves is observed can be explained in terms of Eq. (30). The similarity of the phase curves at different wavelengths means simply that the conditions of quasifractality, $L \propto \lambda$ and $d \propto \lambda$, are approximately satisfied; i.e., the structure of the lunar regolith is nearly the same in some range of scales.

5. LABORATORY PHOTOMETRY

A series of laboratory measurements was carried out for comparison with the lunar data. Two instrument arrangements were used, one for intermediate to large phase angles and another for small phase angles. Measurements presented below were carried out to understand the relative roles of shadow-hiding and interference mechanisms on the lunar phase function.

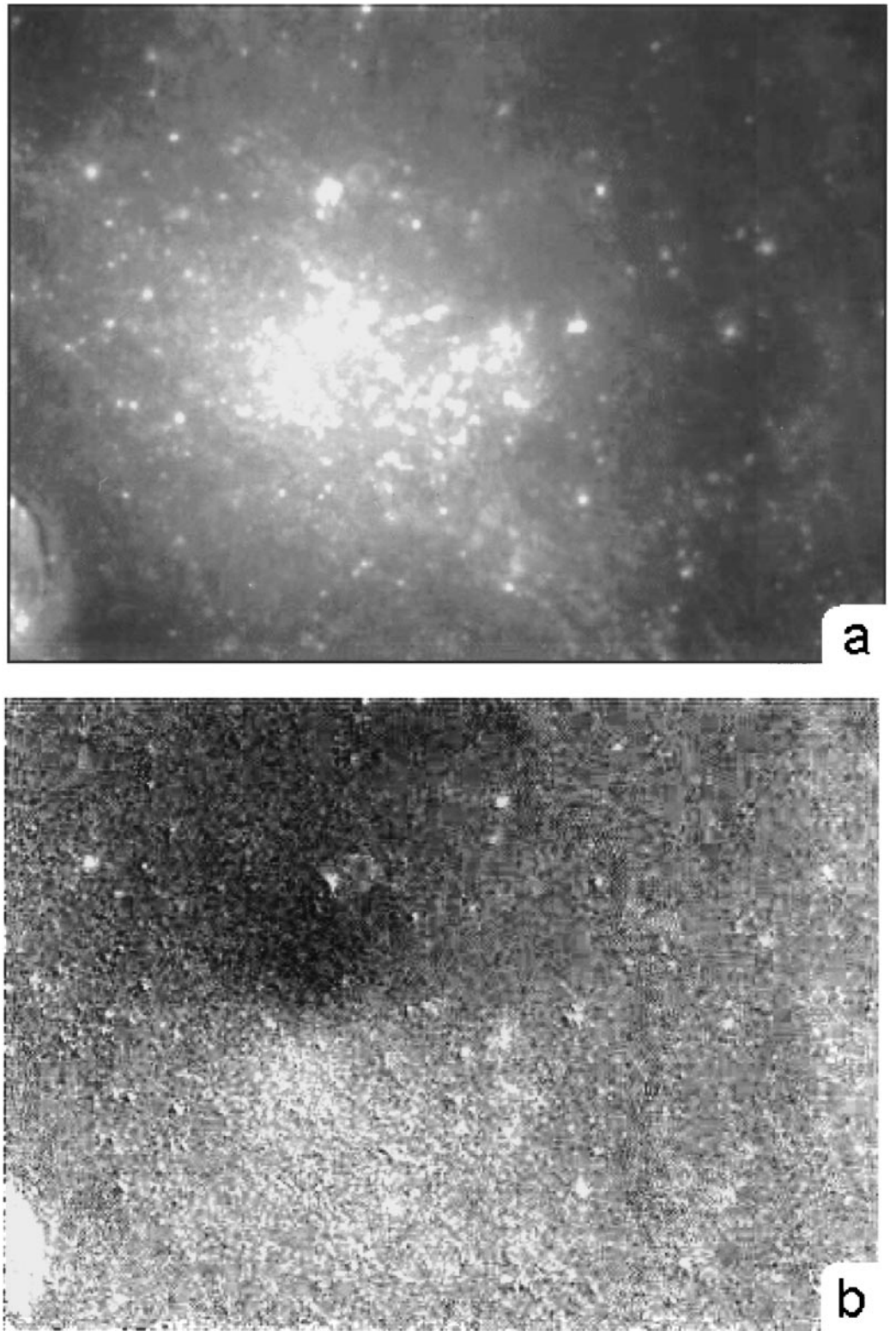

FIG. 9. (a) The Clementine frame LUC2275J.167 showing the opposition spot in northeastern part of Sinus Medii. (b) Ratio of the Clementine images LUD2271J.167 and LUC2275J.167.

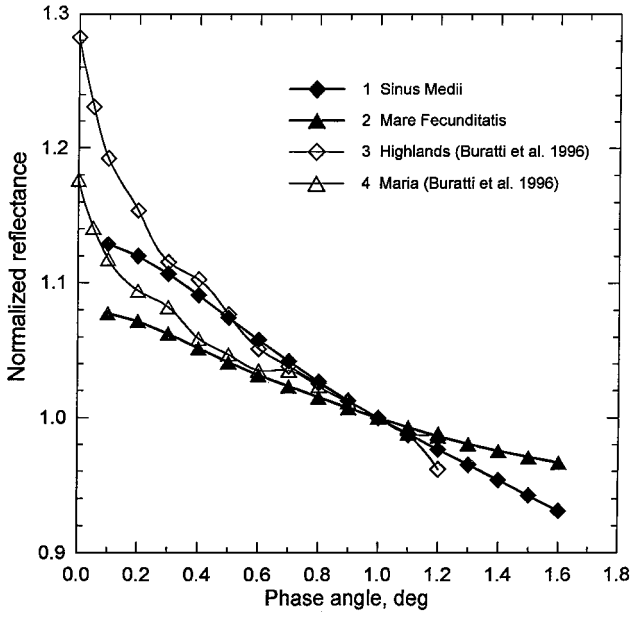

FIG. 10. Near-opposition phase functions derived by the "differential" method for the sites 1.3°N, 3.9°E, Sinus Medii (curve 1), and 1.4°N, 48.7°E, Mare Fecunditatis (curve 2). The phase functions for "average" highland and mare regions (Buratti *et al.* 1996) presented by curves 3 and 4, respectively.

5.1. Measurements in the Phase-Angle Range 3°–45°

The measurements of samples with complicated surface structure were performed at the phase angle range 3°–45° using our laboratory photometer for large phase angles described by Shkuratov and Akimov (1987). Some results have been published by Shkuratov *et al.* (1987, 1989, 1991, 1992). In this series of measurements we used two broad spectral ranges with effective wavelengths of 0.62 μm ($\pm 0.06\,\mu$m) and 0.42 μm ($\pm 0.04\,\mu$m). The apertures of the light source and receiver are equal to 0.5° and 1°, respectively. Thus, smoothing of phase curves by the apertures was small.

Light flux reflected from a bright surface is mainly formed by multiple scattering, which strongly diminishes the shadow-hiding effect. Thus, the interference mechanism dominates the phase function of a bright surface. Figure 13 (open boxes) shows the phase-angle dependence of normalized (at $\alpha = 10^\circ$) reflectance for an even optically thick slab of smoked MgO with albedo nearly 95% (relatively the Halon standard at $\alpha = 5^\circ$). As one can see, a surge in brightness with the amplitude of about 20% occurs in the range of $3^\circ < \alpha < 10^\circ$. The same surge for smoked MgO had been earlier observed by Oetking (1966). A similar surge, but narrower and with smaller amplitude, has also been found for a Halon sample (Shkuratov *et al.* 1989). Since shadows for the bright sample of MgO are nearly absent, the strong peak observed has a largely coherent backscatter origin.

We compared the pure coherent backscatter phase dependence with that of pure shadow hiding. For very dark surfaces multiple scattering is negligible, and shadowing is the only cause of the opposition surge. Figure 13 (black boxes) presents the phase function for soot deposited on an even surface. This sample has an extremely low albedo (about 2.5% with respect to the Halon standard at $\alpha = 5^\circ$). It is remarkable that the phase dependences for soot and MgO almost coincide with each other in this phase angle range, even though the origin of the phase functions is quite different, the former being almost entirely shadow-hiding and the latter being almost entirely coherent backscatter. As will be shown in a later section, at very small phase angles the opposition effects of these two materials is quite different.

Figure 14 presents data for clear glass powders with different sizes of particles and provides another demonstration that coherent backscattering can produce a strong opposition spike. The curves show that the samples with smaller particles have stronger peaks under the same albedos. This behavior is typical of the coherent backscatter origin of the opposition effect (Shkuratov 1985).

Let us consider the wavelength dependence of the opposition spike parameters. The experimental data for MgO and soot surfaces presented in Fig. 13 show that the phase dependences of the color index C(0.6/0.4 μm) is almost absent for both samples. For the soot surface it is not surprising, because shadow hiding does not depend on wavelength. For the MgO surface, we could anticipate some dependence, because the wavelength λ is a parameter in Eq. (30). To explain why the dependence is absent, we can again use the assumption of the quasifractality. This assumption is quite natural for surfaces originated by smoked deposits (Feder 1988), where very small particles form aggregates that in turn are elements of larger aggregates and so on.

There are, nevertheless, surfaces that show conspicuous phase dependences of the color index C(α). As an example, let us consider results of measurements of a powder Fe_2O_3 in two spectral bands (Fig. 15). The powder has very different albedo in red and blue light: 22 and 4%, respectively, at $\alpha = 5^\circ$. At small phase angles the phase curve of this sample in the red light is steeper than in the blue light because of the coherent backscatter enhancement. At larger phase angles the curve in the red light has a gentle slope, because shadow hiding is suppressed by the multiple scattering component and forward scattering of the individual particles is increased with increasing albedo. That can give the minimum of C(α) seen in Fig. 15. The observed increase in the color index (red/blue) with decreasing phase angle around the opposition we call a "color opposition spike" (Shkuratov *et al.* 1996). The phase angle of the color-index minimum could be considered a characteristic of the strength of the coherent backscatter component of the opposition spike. For the powder Fe_2O_3 in red light this angle is very large, about 20°.

Phase-angle dependences of color index (red/blue) for several lunar samples have also been studied (Akimov 1980, Shkuratov *et al.* 1996, Hapke *et al.* 1998). It has been shown that some lunar samples exhibit minimum on the curves at the range 4°–10°. Figure 16 demonstrates data corresponding to our measurements of lunar samples from landing site Luna 24 (coarse 94- to

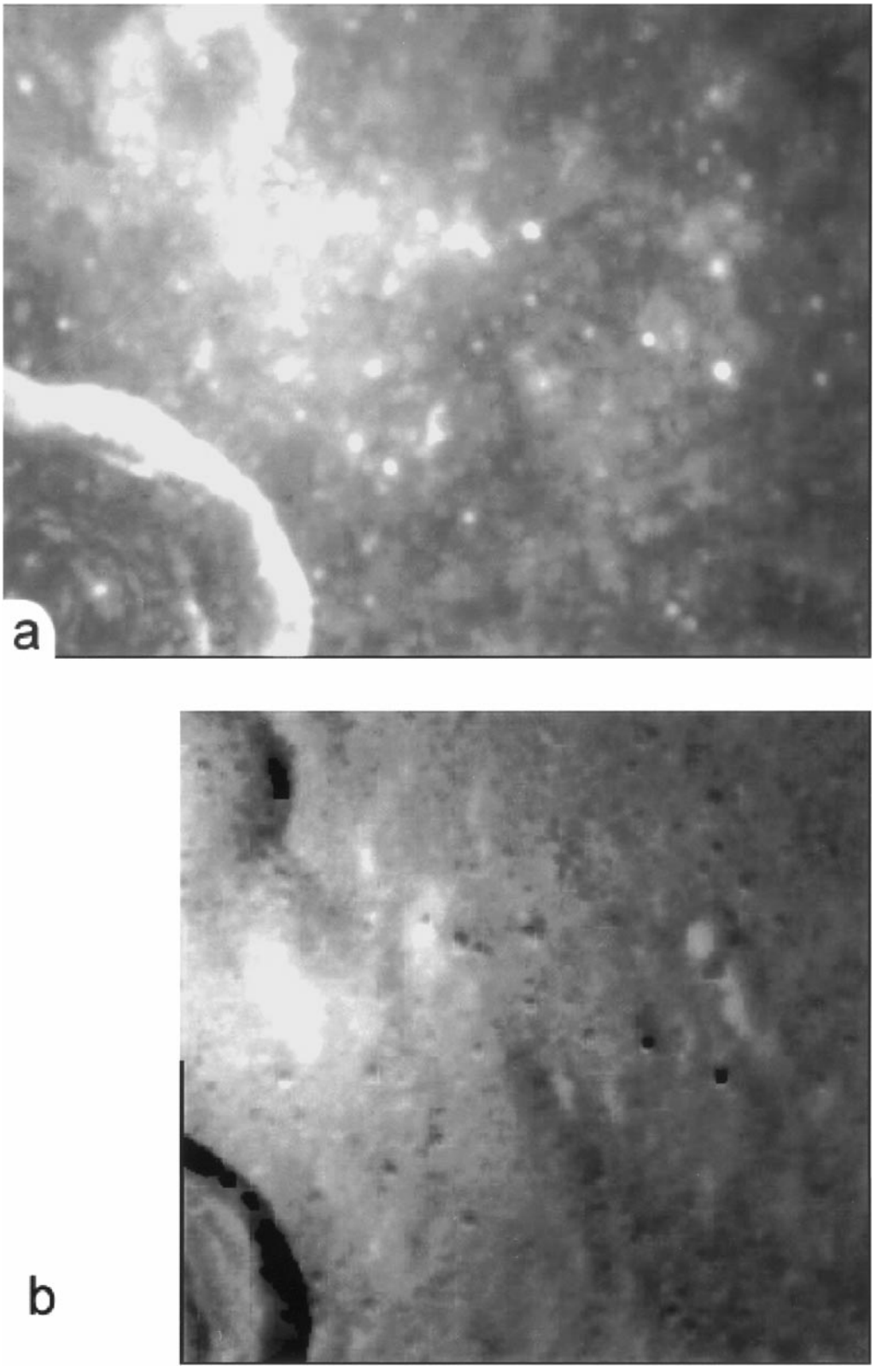

FIG. 11. (a) The Clementine UVVIS frame LUA1983J.168 (0.415 μm). Coordinates of the frame center are 1.4°N and 1.3°E. (b) The ratio of Clementine frames LUA1983J.168 and LUA0598J.300 for the same region.

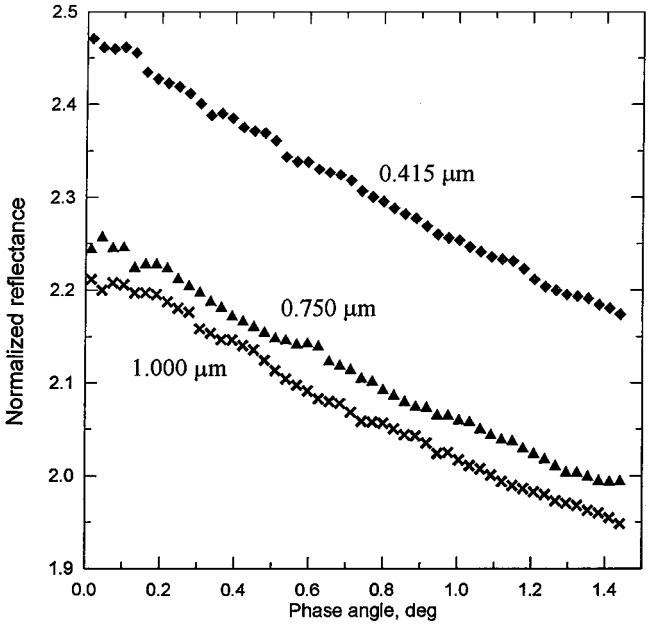

FIG. 12. Near-opposition phase functions derived by the method of phase ratio for the wavelengths 1.000, 0.750, and 0.415 μm. The dependences are normalized at the phase angle of about 26°.

200-μm and fine <74-μm regolith). The fine sample exhibits a minimum of C(α) at about 25°. This phase angle is larger than in the case of coarse regolith. There are lunar samples that do not reveal such a minimum in the range of phase angles 1°–60° (Akimov 1980, Shkuratov *et al.* 1996). No minimum is exhibited also by our analysis of the Clementine data. One explanation of this could be that the conditions of quasifractality are approximately valid for the pristine regolith on the lunar surface, but not for the sorted samples. This may be also related to the fact that the Luna 24 soils are immature.

Thus, data presented in Figs. 13 and 14 show that the coherent backscatter enhancement can contribute the opposition effect in a wide range of phase angles. Moreover, Figs. 15 and 16 evidence that the component can be observed even for comparatively dark surfaces, e.g., for the lunar surface.

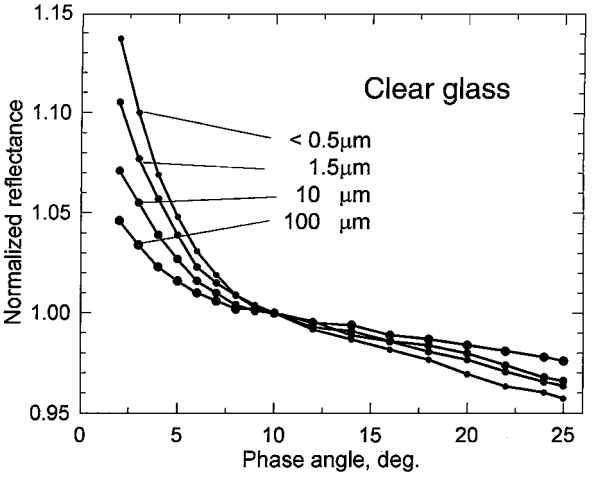

FIG. 14. Normalized reflectance (0.62 μm) phase functions of colorless glass powders with the different average sizes of the particles.

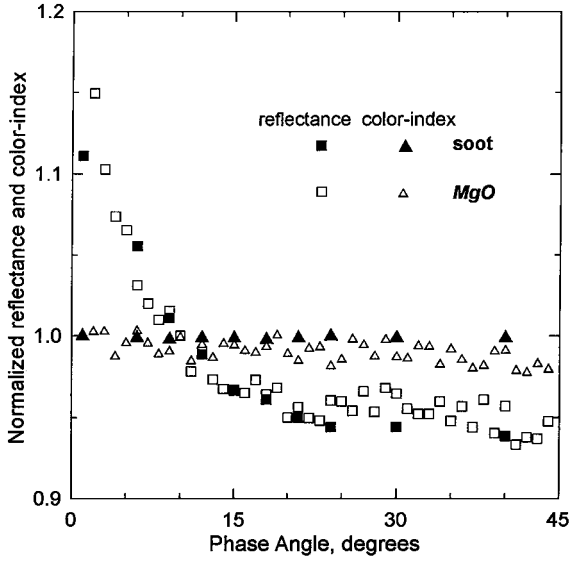

FIG. 13. Normalized reflectance (0.62 μm) (boxes) and color index (0.62/0.42 μm) (triangles) vs phase angle for a "shadow-free" bright surface (sample of MgO) (open symbols) and pure "shadow-hiding" surface (soot smoked deposits on an even background) (black symbols).

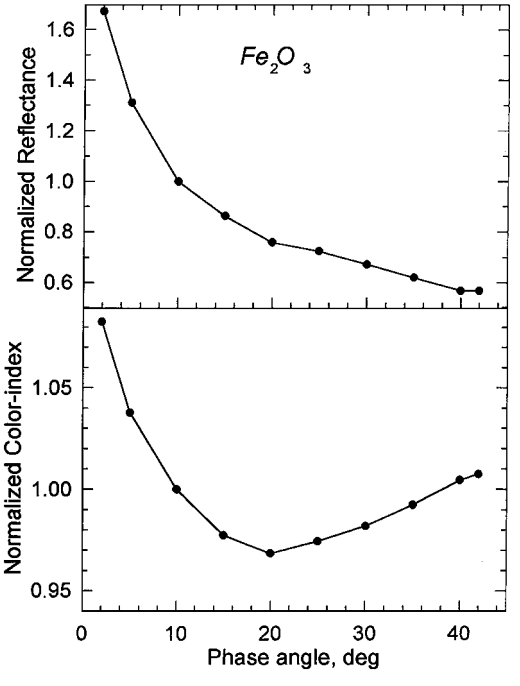

FIG. 15. Normalized reflectance (0.62 μm) and color index (0.62/0.42 μm) vs phase angle for a powder Fe_2O_3.

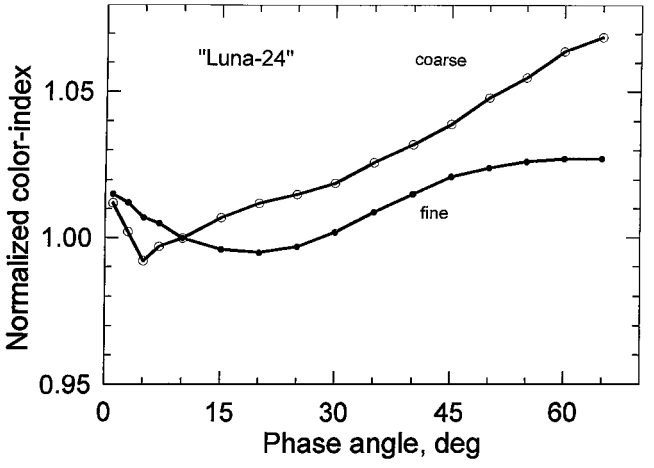

FIG. 16. Color index (0.62/0.42 μm) phase dependences of the lunar samples 24092,4-3,3 (coarse) and 24092,4-1,10 (fine) delivered from the Luna 24 landing site.

5.2. Measurements in the Phase-Angle Range 0.2°–3.5° (Illumination by Nonpolarized Light)

Our laboratory photometer–polarimeter for small phase angles allows measurements in nonpolarized light in the range of phase angles 0.2°–3.5° (Ovcharenko *et al.* 1996, Shkuratov *et al.* 1997b). A halogen lamp is normally used as a source of light in this instrument. We can also use linearly polarized light (see next section). The source and detector angular apertures are 0.05°; therefore, the aperture smoothing of opposition spikes is very small. The instrument permits measurements of samples in a few spectral bands. In this series of measurements we use effective wavelength $\lambda = 0.7\,\mu$m (width $\pm 0.03\,\mu$m) and 0.5 μm (width $\pm 0.05\,\mu$m).

With this instrument we have carried out measurements of the same samples which were studied at larger phase angles (see above). Figure 17 demonstrates the phase-angle dependences of brightness and color index of the sample MgO. As one can see, the sample exhibits not only the wide opposition surge shown in Fig. 13, but also a narrow strong spike. To understand this let us turn to the scheme in Fig. 18. It presents the backscatter on two scales when particles of a medium are aggregates consisting of small grains. In this case, the interference enhancement of rays scattered within and between the aggregates gives rise to the wide and narrow opposition peaks, respectively. If the distribution function of the interference bases is multimodal, phase functions of brightness and/or color index can have some irregularities (Shkuratov *et al.* 1996, 1997b). Note also that this explanation is not the only one: for the broad peak one cannot exclude some influence of the shadow-hiding effect despite very high albedo of the MgO sample.

At small phase angles, $\alpha = 0.2°$–$3.5°$, a significant difference is seen in the brightness and color index phase dependences for the MgO and soot surfaces compared to the larger phase angles (compare Figs. 17 and 19 with Fig. 13). There is a very strong brightness spike near opposition for MgO that is characteristic of coherent backscatter, but only a modest and roughly linear increase for soot that is characteristic of shadow hiding. Unlike the case of large phase angles, the MgO sample shows a small but noticeable phase dependence of color index (about 2%) at the phase angles 0.2°–3.5°. The soot surface does not give any color index dependence.

Our measurements also document a strong particle-size dependence of opposition spike parameters in the phase angle range 0.2°–3.5° for well-sorted quartz samples. Figure 20 demonstrates this effect. The same results have been obtained earlier by Shkuratov *et al.* (1997b) and Nelson *et al.* (1998). Note that Nelson *et al.* measured aluminum oxide powders. These important findings are not consistent with the hypothesis (e.g., Mishchenko 1992, Mishchenko and Dlugach 1992, 1993) that the coherent backscatter enhancement is only observable, if the particle size is of the order of the wavelength. Equation (30) gives a rather good fit to experimental data (see Fig. 20) predicting larger values of L and d for the coarse particle powder. The fitting curves have the following values of the parameters: $k = 0.2$ (both curves), $L = 220\,\mu$m and $d = 90\,\mu$m (for the

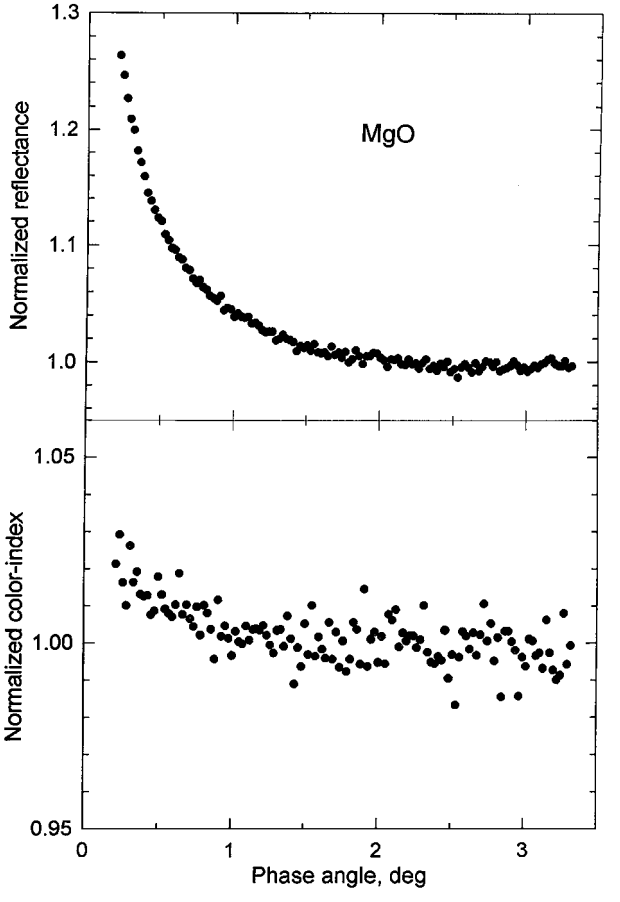

FIG. 17. Normalized reflectance (0.7 μm) and color index (0.7/0.5 μm) vs phase angle for "shadow-free" surface (sample of MgO-smoked deposits on an even background).

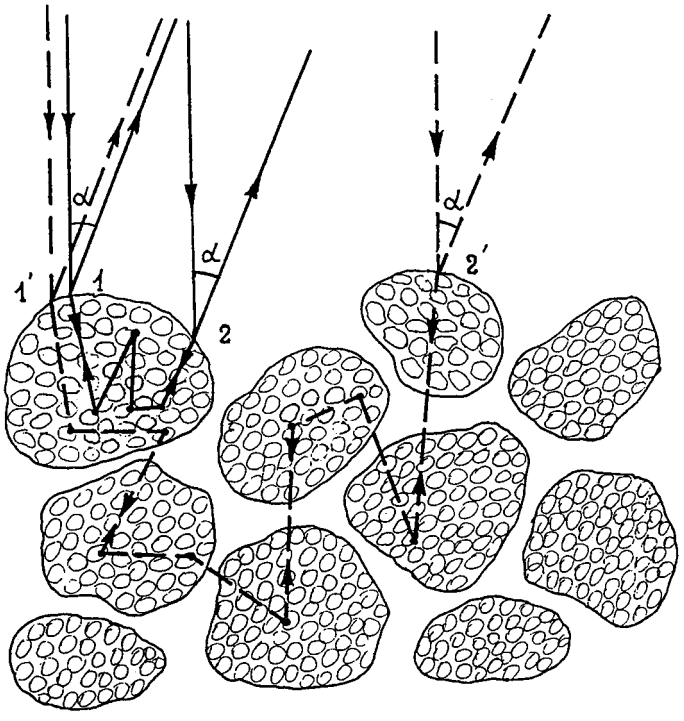

FIG. 18. A scheme of two scale interference opposition spikes.

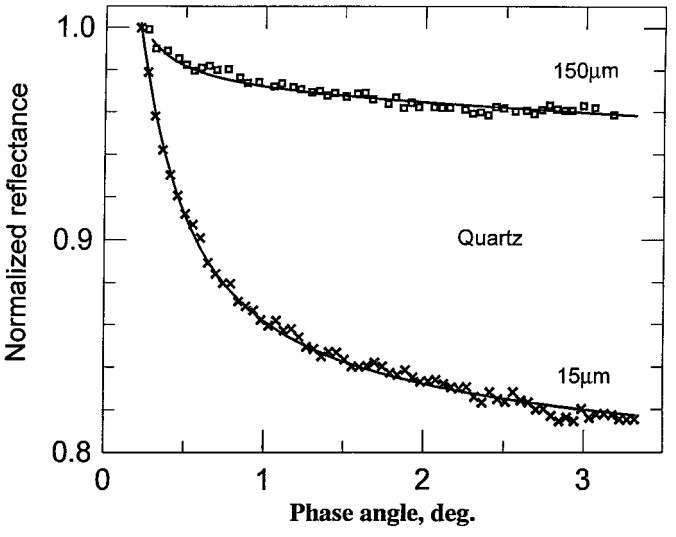

FIG. 20. Normalized reflectance (0.7 μm) of quartz samples with the average size of the particles of 150 and 15 μm. The measurements were performed by the small-phase-angle photometer. The fitting curves calculated by Eq. (30) are also given at the following values of the parameters: $k = 0.2$, $L = 220$ μm, and $d = 90$ μm (for the 150-μm curve) and $k = 0.2$, $L = 29$ μm, and $d = 9.5$ μm (for the 15-μm curve).

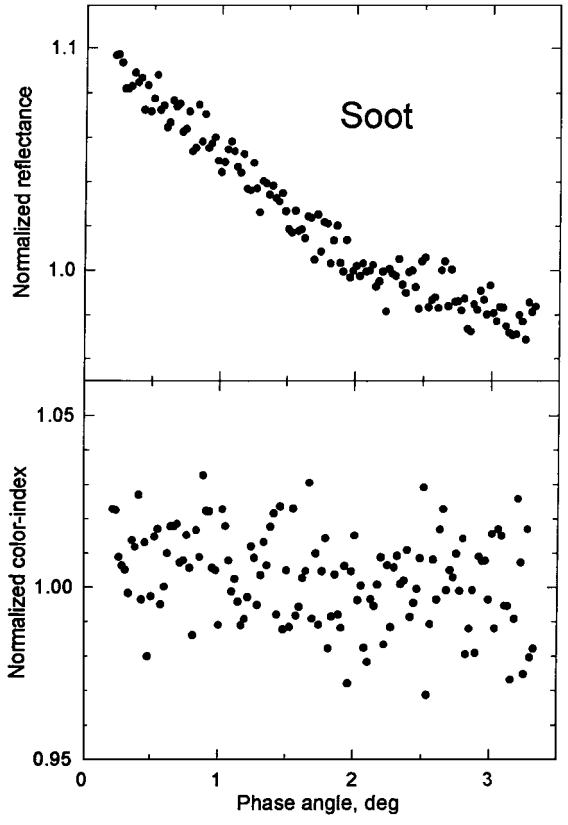

FIG. 19. Normalized reflectance (0.7 μm) and color index (0.7/0.5 μm) vs phase angle for pure shadow-hiding surface (sample of soot smoked on an even background).

150-μm curve), and $L = 29$ μm and $d = 9.5$ μm (for the 15-μm curve). In both cases the values of d are on the order of the particle size. As we have noted above, for structureless particles larger than λ the parameter d should be on the order of the particle size.

Some samples give a minimum on the color index phase curve in the range 0.2°–3.5° similar to that observed for the iron oxide in Fig. 15. Shown in Fig. 21 are examples for palagonites, good spectrophotometric and photometric analogs of Martian soils. The albedos (0.7 μm) of the samples are 18% (left plots) and 33% (right plots) at $\alpha = 3°$. One can see that location of the minimum depends on albedo: the minimum is broader and shifted toward large phase angles for the palagonite sample with low albedo.

It is interesting to compare contributions of single-particle and interparticle scattering in phase function. We have studied a powder of spherical particles of barite colorless glass. The average diameter of spherical particles is of about 50 μm and the refractive index equals 1.45. The albedo of the sample is approximately 110% relative to the Halon photometric standard at $\alpha = 2°$; that means that the opposition spike of the spherical particle powder is stronger than that of Halon. The results of measurements for a monolayer and a thick slab of the spherical particles are shown in Fig. 22. One can clearly see a prominent peak on the phase curve near 0.5°. According to calculations made by Mie's theory (Ovcharenko *et al.* 1996), this peak is a glory ring. The peak is observed both for the thick slab (curve 1) and for the monolayer (curve 2). In the first case the contrast of the glory ring is smaller, which is evidently caused by the masking effect of interparticle scattering. However, the fact that

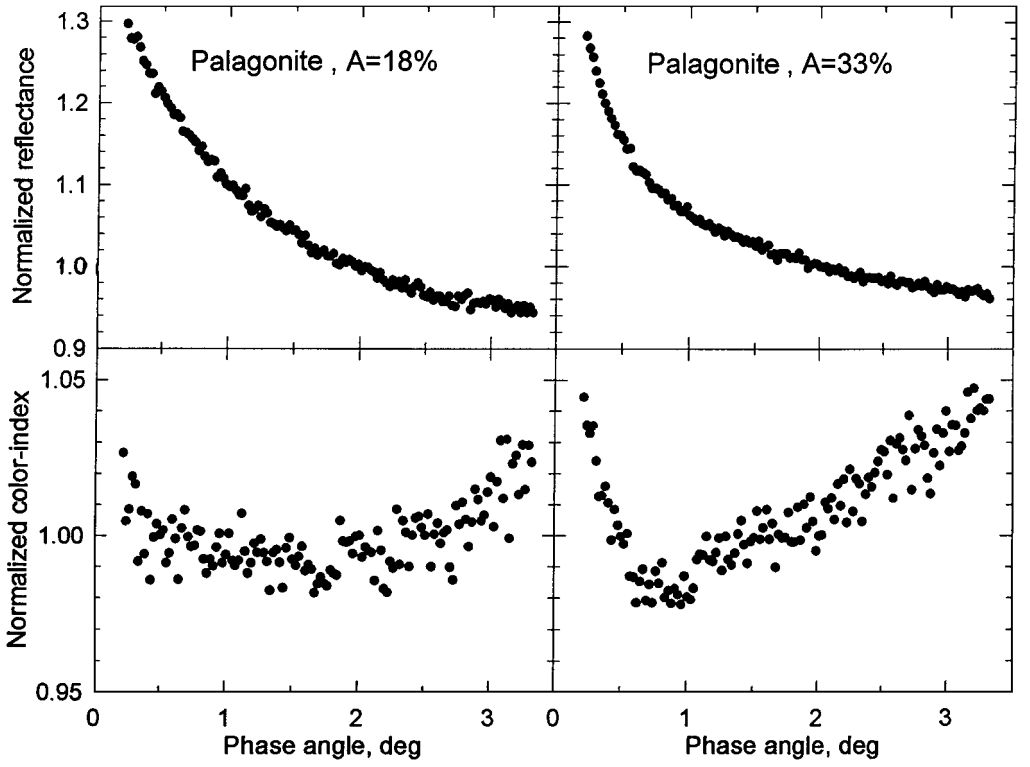

FIG. 21. Normalized reflectance (0.7 μm) and color index (0.7/0.5 μm) phase functions of a palagonite powders measured by the small-phase-angle photometer. The albedos (0.7 μm) of the samples are about 18% (left plots) and 33% (right plots) at $\alpha = 3^\circ$.

we detect this feature for the thick slab shows that even for such a bright surface single-particle scattering can noticeably contribute to the phase dependence of brightness.

Of course, this contribution depends on the size and shape of the particles. If powder particles are significantly smaller than wavelength, the opposition spike of the powder caused by interparticle and even interaggregate scattering should be weak. This can be seen in Fig. 22 (curve 3), which presents data for a quartz powder with particle size about 10 nm. In terms of Eq. (30), for this fine powder the parameter d is larger than L; i.e., the characteristic scale of light diffusion in the surface is less than the dimension of volume for which the cooperative effects of particle interaction are important.

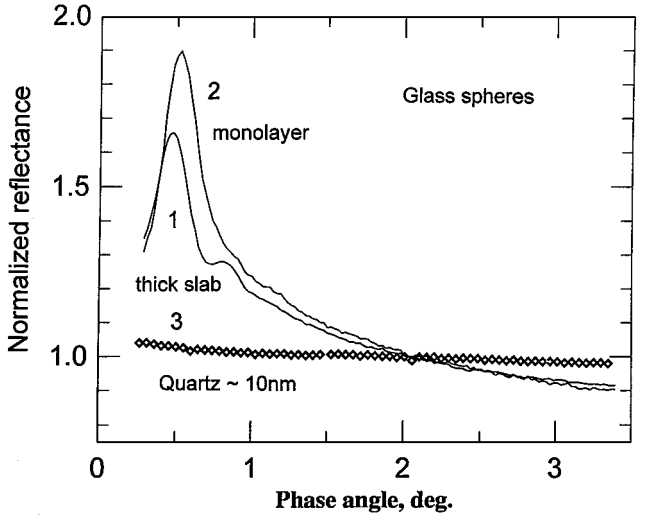

FIG. 22. Normalized reflectance phase dependences (0.7 μm) for a thick slab (curve 1) and a monolayer (curve 2) of spherical particles. The dependence (3) corresponds to quartz powder with submicrometer particles (albedo is about 80% at $\alpha = 3^\circ$).

5.3. Measurements in the Range 0.2°–3.5° (Illumination by Linearly Polarized Light)

To investigate the mechanisms contributing to brightness-phase functions, linear polarized light can be used. This approach was applied by Hapke *et al.* (1993, 1998) to estimate shadow-hiding and interference contributions for lunar samples.

There are four formally independent schemes to measure phase dependences of brightness using linearly polarized light. We denote them (sp), (ss), (ps), and (pp). The first and second letters mark orientations of the polarizer and analyzer axes, respectively. The marks "s" and "p" correspond to the cases when the axes are perpendicular or parallel to the scattering plane, respectively. In the cases (ss) and (pp), the copolarized components of scattered flux are measured. The measurements of the cross-polarized components correspond to the (sp) and (ps) combinations. It is shown (Hapke *et al.* 1998) that combinations (ss) and (pp) exhibit close phase dependences at small enough phase

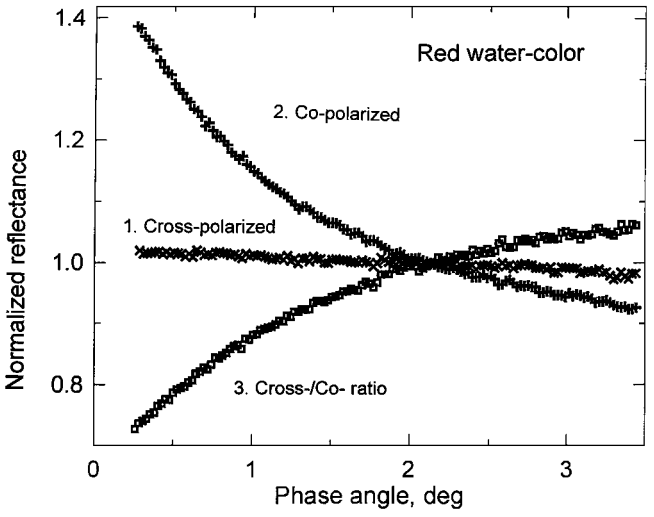

FIG. 23. Normalized reflectance (0.7 μm) phase dependences of cross-polarized (1) and copolarized (2) components for red water color sample with an albedo of 60%. Also shown is the dependence of the normalized cross-/co- ratio (3).

angles. It is true also for the pair (sp) and (ps). Our measurements confirmed these results. We present below phase dependences of co- and cross-polarized components only for the cases (pp) and (ps).

According to Hapke *et al.* (1993, 1998), measurements of co- and cross-polarized components can give information about relative contributions of the shadow-hiding and coherent backscatter effects in the brightness phase functions. The following scheme was suggested. The phase dependence of the copolarized component is contributed by single- and multiple-scattering fluxes, i.e., by both shadow-hiding and coherent backscatter effects, while the cross-polarized component is formed only by multiple scattering, i.e., by the coherent backscatter. Hapke *et al.* (1993, 1998) consider that interference enhancement arises for both components of light polarization. According to this schema the steeper phase behavior of the copolarized component compared to the cross-polarized component implies that the shadow-hiding effect dominates (Hapke *et al.* 1993, 1998). Our measurements and a simple physical consideration presented below show that this schema should be somewhat corrected.

Actually, Eq. (5) shows that the copolarized components for direct and time-reversal trajectories are the same; i.e., at the zero phase angle they always interfere constructively, whereas the cross-polarized components for the trajectories can interfere both constructively and destructively even at pure backscattering. This means that in coherent backscattering, the contribution of the cross-polarized components is smaller than that of the copolarized ones.

Let us consider results of our polarimetric measurements. Figure 23 presents the phase dependences of co- and cross-polarized components of light scattered by a red water color sample (albedo is 60%, at $\lambda = 0.7$ μm). The water color sample was obtained by drying of a water color suspension. Using an optical microscope, we find a surface relief for this sample only on the scales less than 10 μm. Such irregularities are rather transparent in red light. Thus, the surface of the sample was even up to microscales and, hence, the shadow-hiding effect was minimal. As one can see in Fig. 23, the copolarized component has a very prominent peak, whereas the cross-polarized one is almost constant. This is in accordance with the occurrence of the interference enhancement mainly in the copolarized components as required by the reciprocity principle (see Eq. (5)).

According to Hapke *et al.* (1993, 1998), the shadow-hiding effect must be basically revealed in the copolarized components. We agree with this only partially. Indeed, shadowings are effective for large enough fragments of a given medium—when one can neglect their transparency. However, this imports that the shadow-hiding effect contributes both co- and cross-polarized components, since both these components are largely formed in the limits of each fragment. This is confirmed by the following experiment. We used a sample of a hardened cement surface with random "macrorelief" with characteristic slope about 40°. The phase dependences of co- and cross-polarized components were measured for different illumination/observation geometries. If the incidence was along the global normal of the sample ($l = b = 0$), there were no macroscopic shadows on the surface. In this case co- and cross-polarized components (see Fig. 24, curves 3) behave as in the case of the even water color surface (see Fig. 23). When the sample tilts either in the scattering plane ($l = 60°, b = 0$) or in the perpendicular direction ($l = 0, b = 60°$),

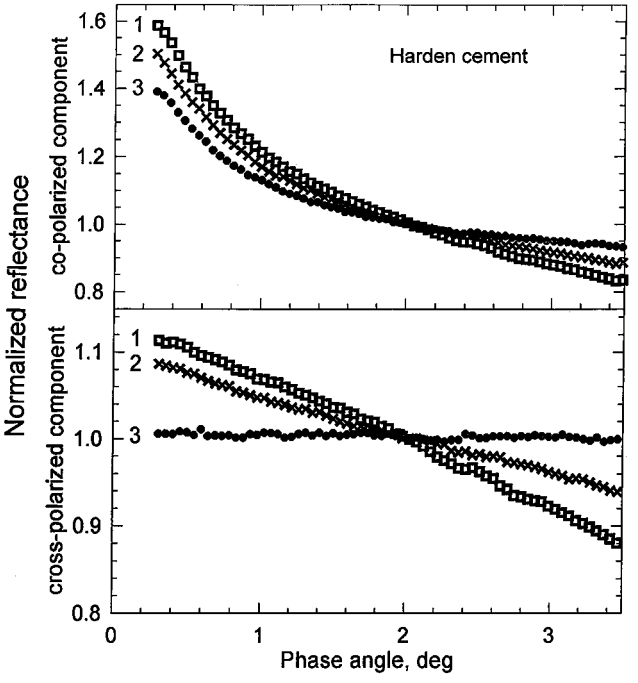

FIG. 24. Normalized reflectance (0.7 μm) phase dependences of copolarized and cross-polarized components for a hardened cement surface with random "macrorelief." Curves 1–3 correspond to the following illumination/observation geometry: ($b = 60°$, $l = 0$), ($b = 0$, $l = 60°$), and ($l = b = 0$), respectively.

shadows appear on the surface of the sample and the shadow effect manifests itself, making brightness phase functions of both co- and cross-polarized components steeper (see Fig. 24). It is interesting to note that if the copolarized curves 1 and 2 are normalized by curve 3, the result practically coincides with the curves corresponding to the cross-polarized components.

For the surface with extremely low albedo the multiple scattering is utterly small and the cross-polarized component can arise only due to asymmetry (anisometry or anisotropy) of individual scatterers. If the surface is formed by densely packed particles with size on the order of the wavelength or less, the single-particle scattering loses the physical sense, since, owing to near-field electromagnetic interactions, scattering by a few particles can be considered as an effective single scatterer giving, generally speaking, cross-polarized components. Figure 25 shows the phase dependences of the normalized cross- and copolarized components measured for a sample of soot smoked on an even surface (albedo is about 2.5% at 3°). Particles of soot have submicrometer sizes and form fuzzy and, in general, asymmetric aggregates. Despite the extremely low albedo of the sample, there is a cross-polarized scattered component, which is about 10 times less intensive than the copolarized one. As one can see in Fig. 25, unlike the dielectric surfaces (Figs. 23 and 24), the smoked soot shows the brightness dependence of cross-polarized component steeper than that of the copolarized one.

Thus, we could consider soot surfaces as a coherent-backscatter-free standard. This standard exhibits the cross-polarized component steeper than the copolarized one (Fig. 25). Any cases when this does not occur we can treat as a presence of the coherent backscatter component.

The different behavior of the cross- and copolarized components for utterly dark and bright materials would be interesting

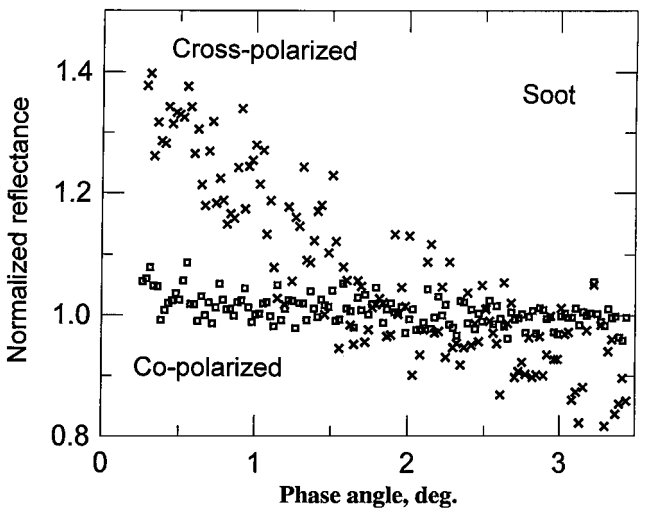

FIG. 25. Normalized reflectance (0.7 μm) corresponding to cross- and copolarized components vs phase angle for soot smoked on an even surface. The cross-polarized component is about 10 times less intensive than the copolarized one.

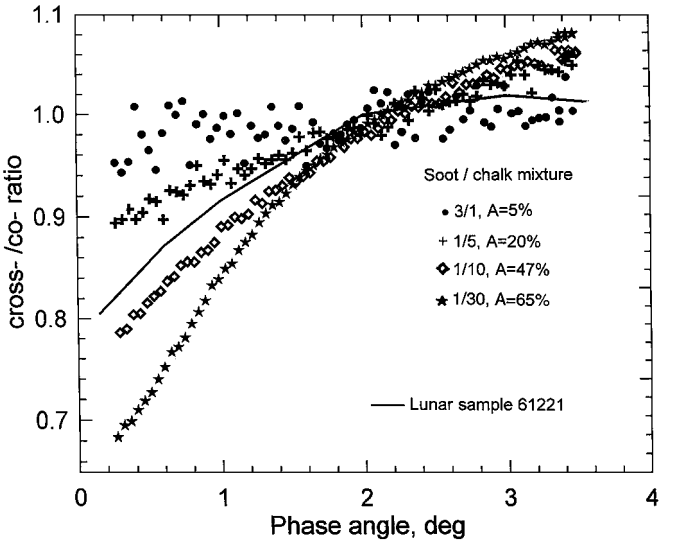

FIG. 26. Ratio of cross- and copolarized components vs α for the lunar sample (61221) (Hapke *et al.* 1998) and mixtures of soot and chalk. The lunar sample is presented by solid curve. Points, crosses, rhombs, and stars correspond to the weight ratios (soot/chalk): 3/1, 1/5, 1/10, and 1/30 with albedos of 5, 20, 47, and 65%, respectively. Our samples and the lunar sample were measured at $\lambda = 0.7$ and 0.633 μm, respectively.

in applications. Figure 26 shows the normalized ratio of cross- and copolarized components (cross-/co- ratio) vs phase angle for mixtures of soot and chalk. The mixture were prepared in water with the following soot/chalk weight ratios : 3/1, 1/5, 1/10, and 1/30. The presented data show that the slope of the phase-angle dependences of the cross-/co- ratio increases as the albedo of the mixture increases. The comparison of Figs. 24 and 26 evidences that even surfaces with albedo of about 5% (points in Fig. 26) have some interference component. This agrees with the conclusion made by Shkuratov *et al.* (1991) that a contribution of the coherent backscatter enhancement can be found even for Phobos, a body darker than the Moon. Figure 26 (solid curve) shows also the phase dependence of cross-/co- ratio for the lunar sample 61221 (Apollo16 landing site) measured by Hapke *et al.* (1998) at $\lambda = 0.633\,\mu$m. The lunar sample has the dependence close to that of the mixture 1/10 with albedo 47% (rhombes). This evidences that the opposition effect of the lunar surface is substantially formed by the coherent backscatter mechanism.

6. CONCLUSION

At the present time, due largely to results of the Clementine mission, interest in photometry of the Moon is experiencing a second birth. A new approach to interpretation of the data is required. We brought together the experimental data (lunar observations and simulating laboratory measurements) and theoretical model deliberately, as such a complex approch seems now to be most fruitful. This approach allows the following comparatively reliable conclusions.

1. We presented a photometric function (30), which combines the shadow-hiding and coherent backscatter mechanisms. We use three nontraditional parameters, which have not been previously exploited. The parameters have rather clear physical sense and the model is simple and gives a good fit to experimental and observational data.

2. Using the average phase dependence of brightness derived from the Clementine data and the photometric model we showed that the best fit is observed when the coherent backscatter contribution is not equal zero. Our calculations indicate that for the Moon the relative contribution of the enhancement is about 15% at the wavelength 0.75 μm and phase angle 3°. Besides, it was shown that the width of the lunar interference surge is up to 10°.

3. The average amplitude of the lunar opposition spike in the range of phase angles 0°–1° is approximately 10%. The Clementine data indicate clearly flattening of phase dependences at phase angles less 0.25° that is a result of the size of the Sun's disk at 1 AU (Shkuratov and Stankevich 1995).

4. Our analysis confirms that no noticeable dependence of lunar brightness phase curves on wavelength is observed at small phase angles. This can be explained by the coherent backscatter mechanism, if one suggests that the ratios $L(\lambda)/\lambda$ and $d(\lambda)/\lambda$, which are the main parameters of the model, are nearly constant over the wavelengths. In other words, we propose that for the Moon the coherent backscatter enhancement is not small, but the changes of λ are practically compensated for by properly changing the characteristic interference base and the size of the volume where the interference mechanism is ineffective. This suggestion is natural, when we assume the lunar regolith to be approximately a quasifractal structure.

5. Results of our laboratory measurements document a broad coherent backscatter surge that can contribute to brightness for phase angles up to 10°. Sometimes, e.g., for the MgO sample, two interference features can be observed: the first (a wide spike) is caused by scattering in particles which are aggregates of submicron dust and the second (a narrow spike) is produced by interparticle scattering. It is interesting to note that phase-angle behavior of the negative polarization, the phenomenon which as well as the opposition spike has the interference origin (Shkuratov 1985), is also unusual for smoke-deposited MgO samples. As has been shown (Lyot 1929, Shkuratov *et al.* 1994b) such samples exhibit characteristics as if two superposed negative branches of polarization were present. These phenomena can be also a result of a superposition of the interference effect at two characteristic scales of surface structure.

6. Often phase dependences of color index reveal a minimum at small phase angles. It can be treated as an indicator of coherent backscatter contribution. For example, such a minimum is characteristic of some lunar samples and optical analogs of Martian grounds (palagonites). Clementine observations have not yet revealed this feature, but this difference may have a theoretical explanation.

7. Our laboratory polarimetric experiments, following the Hapke *et al.* (1998) approach, show that a coherent backscatter component can be important even for surfaces with albedo as low as about 5%. This strengthens evidence that the opposition effect of the lunar surface is partially formed by the coherent backscatter mechanism.

ACKNOWLEDGMENTS

We are grateful to Bruce Hapke and John Hillier for helpful comments on the manuscript. This study was partially supported by CRDF (Grant UG2-295).

REFERENCES

Akimov, L. A. 1975. The effect of mesorelief on the brightness distribution across a planet. *Astron. Zh.* **52**, 635–641. [In Russian]

Akimov, L. A. 1980. On the nature of the opposition effect. *Vestn. Kharkovskogo Univ. Issue 15* **204**, 3–12. [In Russian]

Akimov, L. A. 1988a. *Studies of the Lunar Surface Scattering Low*, Doctor of sciences thesis. Astron. Obs. of Kharkov Univ. Kharkov. [In Russian]

Akimov, L. A. 1988b. Reflection of light by the Moon. 1. *Kinemat. Fiz. Nebesykh Tel* **4**, 3–10. [In Russian]

Akimov, L. A., and Yu. G. Shkuratov 1981. Phase-ratio distributions of the lunar surface in two spectral ranges: Preliminary studies. In *Astronomicheskii Circular*, No. 1167, pp. 3–6. Shternberg State Astron. Inst., Moscow. [In Russian]

Akimov, L. A., I. I. Antipova-Karataeva, and Yu. G. Shkuratov 1979. Indicatrix measurements of lunar samples from landing sites of Luna 24, Luna 16, and Luna 20. In *Lunar Planet. Sci. 10th*, pp. 9–11. LPI, Houston.

Ångström, K. 1885. Ueber Diffusion der strahlenden Warme von ebenen Flachen. *Ann. Phys. Chem.* **26**, 264.

Avanesov, G. A., and 33 colleagues 1991. Results of TV imaging of Phobos (Experiment VSK-Fregat). *Planet. Space Sci.* **39**, 281–295.

Barabashev, N. P. 1922. Bestimmung der Erddalbedo und des Reflexionsgesetzes fur die Oberflache der Mondmeere: Theorie der Rillen. *Astron. Nachr.* **217**, 445–452.

Barabashov, N. P., and A. T. Chekirda 1945. On light reflection by the surfaces of the Moon and Mars. *Astron. J.* **22**, 11–22. [In Russian]

Bowell, E., B. Hapke, D. Domingue, K. Lumme, J. Peltoniemi, and A. Harris 1989. Application of photometric model to asteroids. In *Asteroids II* (R. Binzel, T. Gehrels, and M. Matthews, Eds.), pp. 524–556. Univ. of Arizona Press, Tucson.

Buratti, B. J., J. K. Hillier, and M. Wang 1996. The lunar opposition surge: Observation by Clementine. *Icarus* **124**, 490–499.

Cho, S. 1990. *Electromagnetic Scattering*. Springer-Verlag, New York.

Feder, J. 1988. *Fractals.* Plenum, New York/London.

Fedorets, V. A. 1952. Photographic photometry of the lunar surface. *Uchen. Zap. Kharkovskogo Univ.* **42**, 49–172. [In Russian]

Gehrels, T., T. Coffeen, and D. Owings 1964. Wavelength dependence of polarization. III. The lunar surface. *Astron. J.* **69**, 826–852.

Gnedin, Yu. N., and A. Z. Dolginov 1963. Theory of multiple scattering. *Zh. Eksp. Teor. Fiz.* **45**, 1136–1149. [In Russian]

Hapke, B. 1966. Comments on the paper by Philip Oetking: "Photometric studies of diffusely reflecting surface with application to the brightness of the Moon." *J. Geophys. Res.* **71**, 2515.

Hapke, B. 1971. Optical properties of the lunar surface. In *Physics and Astronomy of the Moon* (Z. Kopal, Ed.), pp. 155–211. Academic Press, New York.

Hapke, B. 1981. Bidirectional reflectance spectroscopy. I. Theory. *J. Geophys. Res.* **86**, 3039–3054.

Hapke, B. 1984. Biderectional reflectance spectroscopy. 3. Correction for macroscopic roughness. *Icarus* **59**, 1–59.

Hapke, B. 1986. Bidirectional reflectance spectroscopy. 4. The extinction coefficient and the opposition effect. *Icarus* **67**, 264–280.

Hapke, B. 1990. Coherent backscatter and the radar characteristics of outer planet satellites. *Icarus* **88**, 407–417.

Hapke, B., R. Nelson, and W. Smith 1993. The opposition effect of the Moon: The contribution of coherent backscatter. *Science* **260**, 509–511.

Hapke, B., R. Nelson, and W. Smith 1998. The opposition effect of the Moon: Coherent backscatter and shadow hiding. *Icarus* **133**, 89–97.

Harris, A., and 12 colleagues 1989. Phase relations of high albedo asteroids: The unusual opposition brightening of 44 Nysa and 64 Angelina. *Icarus* **81**, 365–374.

Helfenstein, P., J. Veverka, and J. Hillier 1997. The lunar opposition effect: A test of alternative models. *Icarus* **128**, 2–14.

Hillier, J. K. 1997. Shadow-hiding opposition surge for a two-layer surface. *Icarus* **128**, 15–27.

Ishimaru, A. 1978. *Wave Propagation and Scattering in Random Media*. Academic Press, New York.

Kravtsov, Yu. A., and A. I. Saichev 1982. Effect of double passage of waves in randomly inhomogeneous media. *Soviet Phys. Uspekhi* **25**, 494–508.

Kreslavsky, M. A., Yu. G. Shkuratov, and V. G. Kaydash 1998. Lunar opposition surge observed by Clementine. *Lunar Planet. Sci. 29th*, 1118.

Kreslavsky, M. A., Yu. G. Shkuratov, and D. G. Stankevich 1997. Lunar phase function from Clementine data: Preliminary results. In *26th International Microsymposium on Comparative Planetology*, pp. 66–67. Vernadsky Institute, Moscow. [Abstract]

Kuga, Y., and A. Ishimaru 1984. Retroreflectance for a dense distribution of spherical particles. *J. Opt. Soc. Am. A* **1**, 831–835.

Lane, A. P., and W. M. Irvine 1973. Monochromatic phase curves and albedos for the lunar disk. *Astrophys. J.* **78**, 267–277.

Lumme, K., and E. Bowell 1981a. Radiative transfer in the surfaces of atmosphereless bodies. I. Theory. *Astron. J.* **86**, 1694–1704.

Lumme, K., and E. Bowell 1981b. Radiative transfer in the surfaces of atmosphereless bodies. II. Interpretation. *Astron. J.* **86**, 1705–1721.

Lyot, B. 1929. Recherches sur la polarisation de la lumiere des planetes et de quelques substances terrestres. *Ann. Obs. Meudon* **8**, 1–161.

Mikhail, J. S. 1970. Color variations with phase of selected regions of the lunar surface. *Moon* **2**, 167–201.

Mishchenko, M. I. 1992. The angular width of the coherent backscatter opposition effect: An application to icy outer planet satellites. *Astrophys. Space Sci.* **194**, 327–333.

Mishchenko, M. I., and J. M. Dlugach 1992. Can weak localization of photons explain the opposition effect of Saturn's rings? *Mon. Not. R. Astron. Soc.* **254**, 15–18.

Mishchenko, M. I., and J. M. Dlugach 1993. Coherent backscatter and the opposition effect for E-type asteroids. *Planet. Space Sci.* **41**, 173–181.

Muinonen, K. 1989. Electromagnetic scattering by two interacting dipoles. In *Proceedings 1989 URSI Electromagnetic Theory Symposium*, pp. 428–430. Stockholm.

Muinonen, K. 1990. *Light scattering by Inhomogeneous Media: Backward Enhancement and Reversal of Polarization*, Ph.D. thesis. University of Helsinki, Helsinki.

Muinonen, K. 1993. Coherent backscattering by solar system dust particles. In *IAU Colloquium 160, Asteroids, Comets, Meteors* (A. Milani, M. DiMartino, and A. Celino, Eds.), pp. 271–296. Kluwer, Dordrecht.

Nelson, R. M., B. W. Hapke, W. D. Smithe, and L. J. Spilker 1998. Experimental tests of models of the coherent backscattering opposition effect. In *Lunar Planet. Sci. 29th*, No. 1146. LPI, Houston.

Nozette, S., and 33 colleagues 1994. The Clementine mission to the Moon: Scientific overview. *Science* **266**, 1835–1839.

Oetking, P. 1966. Photometric studies of diffusely reflecting surface with application to the brightness of the Moon. *J. Geophys. Res.* **71**, 2505–2513.

O'Keefe, J. 1957. Lunar rays. *Astrophys. J.* **126**, 466.

Ovcharenko, A. A., Yu. G. Shkuratov, D. G. Stankevich, and G. Arnold 1996. Laboratory modeling of Europa opposition spike. In *24th International Microsymposium on Comparative Planetology*, pp. 72–73. Vernadsky Institute, Moscow. [Abstract]

Pohn, H. A., H. W. Radin, and R. L. Wildey 1969. The Moon's photometric function near zero phase angle from Apollo 8 photography. *Astrophys. J.* **157**, L193–L195.

Pohn, H. A., R. L. Wildey, and T. W. Offield 1971. Correlation of the zero-phase brightness surge (heiligenschein) with lunar-surface roughness, Appollo 14 Prelim. Sci. Rep. Part F. NASA SP-272

Rougier, G. 1933. Photometrie photoelectrique global de la Lune. *Ann. Obs. Strasburg* **2**, 205–399.

Shkuratov, Yu. G. 1983. A model of the opposition effect in the brightness of airless cosmic bodies. *Soviet Astron.* **27**, 581–583.

Shkuratov, Yu. G. 1985. On the origin of the opposition effect and negative polarization for cosmic bodies with solid surface. In *Astronomicheskii Circular*, No. 1400, pp. 3–6. Shternberg State Astron. Inst., Moscow. [In Russian]

Shkuratov, Yu. G. 1988. A diffraction mechanism of brightness opposition effect of surfaces with complicated structure. *Kinemat. Fiz. Nebesnykh Tel* **4**, 33–39 [In Russian]

Shkuratov, Yu. G. 1989. Interference mechanism of opposition spike and negative polarization of atmosphereless planetary bodies. *Bull. Am. Astron. Soc.* **21**, 989.

Shkuratov, Yu. G. 1991. Estimating the effect of angular light source dimensions on the opposition brightness effect of atmosphereless bodies. *Sol. Syst. Res.* **25**, 54–57.

Shkuratov, Yu. G. 1995. Fractoids and photometry of solid surfaces of celestial bodies. *Sol. Syst. Res.* **29**, 421–432.

Shkuratov, Yu. G., and L. A. Akimov 1987. Laboratory investigations of negative polarization of light scattered by surfaces with complicated structure. Some consequences for atmosphereless celestial bodies. 1. *Kinemat. Fis. Nebesnykh Tel* **3**, 22–27. [In Russian]

Shkuratov, Yu. G., and M. A. Kreslavsky 1998. A model of lunar photometric function. In *Lunar Planet. Sci. 29th*, No. 1117. LPI Houston.

Shkuratov, Yu. G., and A. A. Ovcharenko 1998. Brightness opposition effect: A theoretical model and laboratory measurements. *Sol. Syst. Res.* **32**, 276–286.

Shkuratov, Yu. G., and D. G. Stankevich 1995. Can lunar opposition spike measured by Clementine exist? In *Lunar Planet. Sci. 26th*, pp. 1295–1296. LPI, Houston.

Shkuratov, Yu. G., L. A. Akimov, N. P. Stankevich, L. Ya. Melkumova, I. I. Latinina, and T. B. Bogdanova 1987. Laboratory investigations of negative polarization of light scattered by surfaces with complicated structure: Some consequences for atmosphereless celestial bodies. 2. *Kinemat. Fis. Nebesnykh Tel* **3**, 32–37. [In Russian]

Shkuratov, Yu. G., A. S. Kachanov, and V. S. Karpov 1989. Photometry and polarimetry the photometric standard PTFE (Halon) at small phase angles. In *Astronomicheskii Circular*, No. 1538, pp. 47–48. Shternberg Astron. Inst., Moscow. [In Russian]

Shkuratov, Yu. G., M. A. Kreslavsky, and D. G. Stankevich 1997a. On the lunar opposition spike observed by Clementine: New results. In *Lunar Planet. Sci. Conf. 28th*, pp. 1307–1308. LPI, Houston.

Shkuratov, Yu. G., L. Ya. Melkumova, N. V. Opanasenko, and D. G. Stankevich 1996. Phase dependence of the color indices of solid surfaces of celestial bodies. *Sol. Syst. Res.* **30**, 71–79.

Shkuratov, Yu. G., N. V. Opanasenko, A. T. Basilevsky, B. S. Zhukov, M. A. Kreslavsky, and S. Murchie 1991. A possible interpretation of bright features on the surface of Phobos. *Planet. Space Sci.* **39**, 341–347.

Shkuratov, Yu. G., N. V. Opanasenko, and M. A. Kreslavsky 1992. Polarimetric and photometric properties of the Moon: Telescope observation and laboratory simulation. 1. The negative polarization. *Icarus* **95**, 283–299.

Shkuratov, Yu. G., A. A. Ovcharenko, D. G. Stankevich, and V. V. Korokhin 1997b. A study of light backscattering from planetary-regolith-type surfaces at phase angles 0.2–3.5 degrees. *Sol. Syst. Res.* **31**, 56–63.

Shkuratov, Yu. G., D. G. Stankevich, A. A. Ovcharenko, L. V. Ksanfomaliti, E. V. Petrova, and G. Arnold 1998. Amplitude of the martian opposition effect derived from "Phobos-2" data. *Sol. Syst. Res.* **32**, 90–98.

Shkuratov, Yu., L. Starukhina, M. Kreslavsky, N. V. Opanasenko, D. G. Stankevich, and V. G. Shevchenko 1994a. Principle of perturbation invariance in photometry of atmosphereless celestial bodies. *Icarus* **109**, 168–190.

Shkuratov, Yu. G., and 10 colleagues. 1994b. A critical review of theoretical models for the negative polarization of light scattered by atmosphereless Solar System bodies. *Earth Moon Planets* **65**, 201–246.

Shorthill, R. W., J. M. Saari, F. F. Baird, and J. R. LeCompte 1969. *Photometric Properties of Selected Lunar Features*, NASA Contractor Report CR-1429.

Stankevich, D. G., Yu. G. Shkuratov, and K. Muinonen 1999. Shadow-hiding effect in ingomogeneous and layered particulate media. *J. Quant. Spectrosc. Radiat. Transfer*, in press.

Thompson, D. T., and G. W. Lockwood 1992. Photoelectric photometry of Europa and Callisto. *J. Geophys. Res.* **97**, 14,761–14,772.

Watson, K. M. 1969. Multiple scattering of electromagnetic waves in an underdense plasma. *J. Math. Phys.* **10**, 688–702.

Whitaker, E. A. 1969. An investigation of the lunar heiligenschein. In *Apollo 11 Preliminary Science Report*, NASA SP-201, pp. 38–39.

Wildey, R. L. 1972. Physical and geological aspects of heiligenschein measurements. In *Apollo 16 Preliminary Science Report*, NASA SP-315, pp. (29) 113–(29)119. Washington, DC.

Wildey, R. L. 1978. The Moon in heiligenschein. *Science* **200**, 1265–1267.

Zhukov, B. S., and 14 colleagues 1994. Photometric characteristic of Phobos and their interpretation. In *TV-Investigation of Phobos* (G.A. Avanesov *et al.*, Eds.), pp. 80–94. Nauka, Moscow. [In Russian]